Journal of Sound and Vibration 596 (2025) 118786

Contents lists available at ScienceDirect

Journal of Sound and Vibration

journal homepage: www.elsevier.com/locate/jsvi

Acoustic flow resonances in installed rectangular jets

V.A. Shorstov [a], S.A. Karabasov [b,*], V.E. Makarov [a], A.K. Mironov [a], V. Gryazev [c]

[a] Central Institute of Aviation Motors (CIAM), Moscow, Aviamotornaya str., 2, Russia
[b] School of Engineering and Materials Science, Queen Mary University of London, Mile End Road, London, E1 4NS, UK
[c] Department of Mechanical and Aerospace Engineering, Brunel University London, Kingston Lane, Uxbridge, UB8 3PH, UK

ARTICLE INFO

Keywords:
Jet installation noise
Acoustic flow resonance
large eddy simulation

ABSTRACT

Zonal Large Eddy Simulations (LES) of complex installed rectangular jet flows are performed for subsonic jet conditions of the Central Institute for Aviation Motors (CIAM) experiment, where a strong tone was reported. For far-field noise modelling, the zonal LES solutions are coupled with the permeable formulation of the Ffowcs Williams and Hawkings (FW-H) method. The obtained noise spectra predictions are compared with the acoustic measurements in the CIAM facility. To reduce statistical noise of the relatively short LES time series, contributions due to several dominant low frequency tones and the remaining broadband signal are computed separately, using a tailored Fourier transform technique for each signal type. For cross-validation, noise spectra measurements of an equivalent isolated round jet in the CIAM facility are compared with the empirical sJet model calibrated on the NASA Small Hot Jet Acoustic Rig (SHJAR) jet noise database. While the two datasets agree reasonably well for mid to high frequencies, larger discrepancies are observed for low frequencies, which are attributed to acoustic reflections in the non-anechoic CIAM facility. The differences in noise levels between the CIAM dataset and the sJet model representing the NASA jet noise data are used to determine the experimental uncertainty of the CIAM noise measurements for each frequency and observer angle. For the installed rectangular jet, it is shown that far-field noise spectra predictions of the zonal LES-FW-H method for both the fundamental tone, its sixth harmonic corresponding to the jet Strouhal number of around 1, and the broadband component are broadly within the experimental error bar for most observer angles. Some discrepancies between predictions of the zonal LES method and the CIAM measurements for the main low frequency tone for the 30° and 90°, where the experimental uncertainty at low frequencies is largest are also noted. After validating the acoustic solutions, spectral and conditional averaging analysis methods are applied to elucidate mechanisms of the acoustic-flow resonance in the installed rectangular jet flow. The numerical dispersion relation is obtained to analyse phase velocities of the upstream and downstream travelling pressure waves in the stream-wise direction. The conditional analysis of pressure fluctuations inside the jet reveals the emergence of internal reflection points corresponding to a rapid change of the acoustic wave phase as well as the saddle points interpreted as localised zones of vorticity shed from the side-wall edges. To independently investigate the effect of trailing edges and corner points of the jet embodiment geometry on closing the acoustic-flow resonance cycle, several modifications of the baseline rectangular nozzle are considered, such as introducing chevron-like lobes and cuts on the trailing edges of the side walls as well as smoothing the sharp corner points of the wall edges. Following the series of additional zonal LES runs with the modified installed nozzle geometries, an optimized tone-less modification of the original installed nozzle was obtained, in broad agreement with the conditional analysis results. The obtained tone-less modification of the

* Corresponding author.

https://doi.org/10.1016/j.jsv.2024.118786
Received 20 May 2023; Received in revised form 17 October 2024; Accepted 21 October 2024
Available online 28 October 2024

installed rectangular jet is further analyzed to provide insights into its similarity and differences from the aeroacoustics of the reference isolated round jet in the same CIAM facility.

1. Introduction

Acoustic properties of jet flows interacting with surfaces have attracted significant attention in the literature. Recently, the interest in jet flow interaction with airframe was inspired by modern tightly coupled airframe-jet engine concepts [1] as well as traditional 'pipe-under-the -wing' jet exhaust configurations [2,3]. Since 1970s, noise generated by propulsive jets has been known to be modified in the presence of solid surfaces, where the additionally generated noise was termed installed jet noise [4,5]. A common feature of the jet interacting with surfaces is the generation of tones in the far-field noise spectra. Such tones generated in canonical installed jet configurations, e.g. when a round jet interacts with a flat plate, were extensively studied in the literature, starting from the early works [6-8], and to more recent investigations [9,10]. For the jet-flat-plate configuration, a feedback loop is known to form between the upstream condition at the nozzle exit and the plate trailing edge, thereby leading to the so-called edge tone phenomenon [10]. In the latter case, the tone generation mechanism can be explained by the fact that the early shear layers of a jet close to the nozzle exit are receptive to Kelvin-Helmholtz instability waves, which propagate downstream and interact with the plate trailing edge. The latter interaction generates upstream-travelling acoustic waves, which, in turn, excite the early shear layers, thereby closing the resonance loop. In addition to the tone generation due to the nozzle lip/trailing edge resonance mechanism, the acoustic feedback loop with the trailing edge can also be closed by internal reflection points inside the jet. For example, these internal points may occur due to the acoustic waves reflecting from the spreading jet shear layers, by analogy with acoustic reflections in a duct with soft wavy walls [11]. As shown in [11], for isolated circular jet flows, the internal reflection points correspond to saddle points of the roots of the dispersion relation of linearised Euler equations, which can be computed semi-analytically. At the same time, in comparison with the canonical circular jet/flat plate configuration, resonances due to 3D acoustic/flow interactions, which occur in tightly coupled airframe-non-axisymmetric jet configurations are much less studied. Moreover, to the best knowledge of the authors, only a handful of publications have considered non-axisymmetric jet flows in the context of jet installation noise so far. For example, acoustic-flow interactions of a rectangular subsonic jet installed above a flat plate were investigated in [12]. This work showed that resonances in installed rectangular jets show considerable differences in comparison with edge-tone phenomenon in round jets even for the simple flat plate case. During the resonance cycle, the rectangular jet was shown to exhibit large contortions typical of 3D acoustic-flow interaction effects. In a recent experimental study [13], several circular chevron jets installed above a flat plate with a porous trailing edge were considered. The plate was placed at a sufficient distance from the jet to exclude direct jet flow-flat plate interaction. For a coarse-pore trailing edge treatment, acoustic tones were reported in the far-field noise spectrum, which were attributed to a resonance loop developing between the nozzle exit and the junction point between solid and flow-permeable surfaces of the plate. A further complex installed jet configuration was considered in the experimental work by NASA [14], where a rectangular subsonic jet was considered in two embodiments. In the first case, the embodiment comprised the nozzle lip extended to a flat plate section confined by triangular side walls, and the second case considered the nozzle merged with a semi-infinite flat plate. It both cases, a considerable additional jet installation noise was observed compared to the isolated configuration of the same rectangular jet. In the subsequent work [15], several rectangular nozzles in different embodiments were tested, showing additional noise generated in comparison with the baseline rectangular nozzle especially at low frequencies. It was also demonstrated that the low frequency noise could be reduced by replacing the baseline single stream rectangular nozzle by a multi-stream nozzle, thereby changing the upstream reflection point condition.

For investigation of complex wall-bounded flows typical of rectangular jets in embodiments such as considered in the NASA experiments [14,15], high-resolution unsteady Computational Fluid Dynamics (CFD) methods are required. In particular, Large Eddy Simulations (LES) can provide a wealth of space-time resolved information about the turbulent jet flow including the acoustic wave propagation effects.

For single-stream circular jets installed about a flat plate, good progress has been obtained in applying Large Eddy Simulations to consistently predict far-field noise spectra within 1–2 dB from the experiment for a range of operational jet conditions and frequencies [16]. In the latter example, a Very Large Eddy Simulation (VLES) approach was used based on the Lattice Boltzmann (LBM) method with a wall model, which required an LES mesh of 942 million voxels. Another example of state-of-the-art Wall-Modelled LES (WMLES) methods for jet flow and noise modelling is the high-resolution Compact Accurately Boundary-Adjusting high-REsolution Technique (CABARET) [17] accelerated on Graphics Processing Units (GPUs) [18]. In [19], GPU-CABARET was applied to compute an installed non-axisymmetric jet flow solution for the industrial-style geometry, which included a co-axial nozzle, a pylon, and a wing with a flap, and a part of the fuselage on LES meshes up to 243 million cells. Furthermore, by carefully adjusting the upstream inflow conditions for a class of isolated circular jet flows in state-of-the-art LES jet models [20,21], an impressive accuracy of noise spectra predictions within 1 dB from the experimental measurements was reported for a range of observer angles and frequencies.

Notwithstanding the general progress in jet LES, for complex installed non-circular jets, pure LES methods can still be prohibitively expensive, unless crucial trade-offs are made to reduce the 3D complexity. For example, in [22] a reduction of the span-wise domain size was required to obtain a converged LES solution for a rectangular jet installed above a flat plate. At the same time, hybrid Reynolds Averaged Navier Stokes (RANS) - LES methods have reached a mature state for eddy-resolving modelling of wall-bounded jet flows of industrial complexity [23]. In the present work, a representative of the latter class of methods, a zonal Unsteady RANS (URANS)-LES approach has been used, which can utilise coarser meshes compared to the Wall Modelled LES approaches. Details of the numerical

approach can be found in [24-28]. Briefly, the URANS equations are solved together with the Spalart–Allmaras turbulence model. For capturing both the tonal and broadband noise components, the URANS equations are coupled with LES in the areas where the numerical grid resolution is sufficient, using an improved synthetic turbulence generator, which was specifically designed for aeroacoustic problems by Shur and co-workers [28]. In previous works [26,27], the implemented hybrid RANS-LES method was validated for problems of noise generated by boundary layer flows. The suggested zonal approach was shown to be sufficiently flexible to adapt the complexity of the computational scheme by changing the size of the RANS zone as required by the physics.

The focus of the current work is the acoustic-flow interaction phenomenon reported in the recent installed jet experiment performed in the CIAM open-stand aeroacoustic facility [29]. In the CIAM experiment, a rectangular nozzle is considered, where the lower lip is extended to a deck confined by side walls of winglet-type shapes representing a tightly coupled jet exhaust-airframe configuration (Fig. 1). To reduce the effect of the ground reflections from the noise measurements in the open-stand facility, the jet rig stand was elevated by 2.61 m with respect to the ground. For acoustic measurements, the microphones were positioned on an arc of 3 m from the ground and at 6 m from the nozzle exit using the traverse system. To change the observation plane relative to the installed jet, the rectangular nozzle was rotated relative to the microphone system in the jet azimuthal direction. In addition, for comparison with the installed jet results, the installed rectangular nozzle was replaced by a reference isolated round nozzle in the same acoustic rig. The isolated round jet had the same equivalent diameter and the same plenum pressure and temperature conditions as the installed rectangular jet. To quantify the effect of wall and ground reflections on acoustic measurements in the CIAM experiment, as a part of the current work, results of the noise spectra measurements of the isolated round jet will be compared with the NASA SHJAR jet noise database [30,31].

The paper is organized as follows:

In Section 2, the experimental and computational models are introduced. Section 3 presents the flow and far-field noise results of the installed rectangular jet modelling, which are compared with the acoustic measurements in the CIAM facility. For evaluation of the experimental uncertainty, the CIAM noise measurements of the equivalent isolated round jet at the same upstream total pressure and temperature conditions are compared with the empirical sJet model [31], which is based on scaling laws calibrated on the NASA SHJAR jet noise database. Following the validation of acoustic results, the spatio-temporal pressure fluctuations in the installed rectangular jet are analyzed using the spectral and conditional averaging techniques to provide insights into the acoustic-flow interaction cycle, leading to tones in the far-field noise spectra. In Section 4, for the same upstream jet conditions, several modifications of the embodiment of the baseline rectangular nozzle are considered, and the corresponding changes in the jet flow regime are simulated using the zonal LES method. The resulting optimized tone-less geometry, where the acoustic reflections from the side-wall edges are removed, are further analyzed to provide additional insights on broadband noise sources.

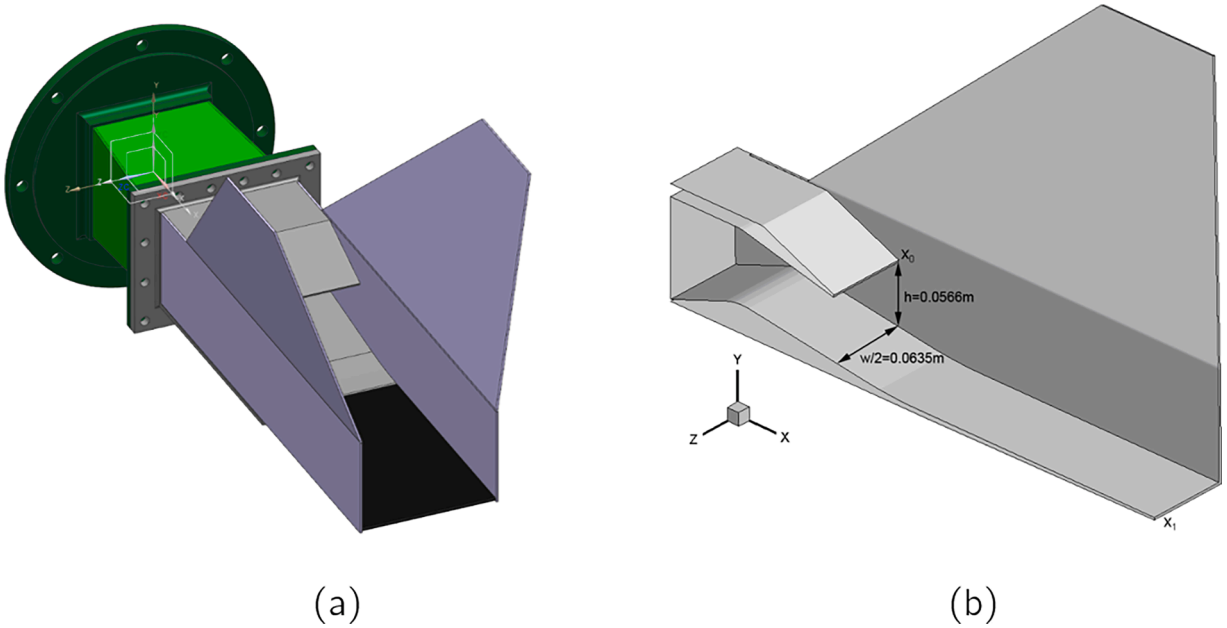

Fig. 1. A schematic of the installed rectangular jet setup from the CIAM experiment: (a) full view and (b) side view on ½ of the model cut in the symmetry plane. Points x_0 and x_1 are the stream-wise coordinates of the nozzle lip and the trailing edge of the plate. h and w correspond to the height and width of the rectangular nozzle at $x = x_0$.

2. The experimental setup and computational methods

2.1. Far-field noise measurements in the CIAM facility

The experiment was performed in an open acoustic facility C17-A4 [29]. Fig. 2 shows a schematic of the acoustic rig. The rectangular nozzle model, which had been originally designed for dual-stream jets, was adjusted to a single-stream jet flow by blocking the internal stream with a filler, whilst keeping the external stream open. The air heated by a flame combustor was supplied from the upstream plenum at a Nozzle Pressure Ratio (NPR) of 1.682 and total temperature (T_0) 505 K, which corresponds to a heated jet at an acoustic Mach number of 0.894. The nozzle was mounted at a distance of 3 m above the hard floor (asphalt), which was assumed to be sufficiently large in comparison with the nozzle diameter (0.1 m) to avoid significant reflections from the ground. To test validity of this assumption in the current work, noise measurements of an isolated jet in the CIAM will be compared with the NASA jet noise database in Section 3.3. The isolated jet setup and the NASA database are briefly discussed at the end of this Section.

Acoustic microphones were placed at a distance of 6 m from the nozzle exit and at the same distance from the ground as the nozzle, which approximately corresponds to the geometric acoustics far-field region of the jet flow. The polar angle, θ measured between the microphone location and the jet axis was varied using the traverse system. Positive values of the polar angle correspond to the reflected side of the installed jet.

By rotating the nozzle around the horizonal axis (x-axis in Fig. 1), noise measurements were performed in the symmetry plane of the model and in the lateral plane of the nozzle. Only the symmetry plane dataset will be used in the present work.

Before testing the installed rectangular nozzle, a reference isolated round single-stream nozzle was tested in the same acoustic rig. The round nozzle was convergent and had a profiled-wall geometry. The effective exit diameter of the rectangular nozzle by area corresponds to $D_j = 0.0957$ m, which is about 13.5 % smaller than that of the round nozzle. Hence, a suitable scaling factor will be used when comparing the two jet noise datasets in Section 4. For cross-validation, the acoustic spectra of the round nozzle will be compared with noise predictions of the empirical NASA sJet model [31]. The sJet model was calibrated for a large number of NASA jet cases, thereby representing the NASA consensus jet noise dataset for the same total pressure and temperature conditions as in the CIAM experiment.

2.2. Computational models

A rectangular computational domain is considered, where the stream-wise length corresponds to 38 heights of the rectangular nozzle. The span-wise and wall-normal sizes of the computational domain are approximately equal to 33 nozzle heights. Hybrid RANS-based boundary conditions are applied on all solid walls, and characteristic non-reflective boundary conditions are imposed on the lateral and downstream boundaries. Upstream of the nozzle exit, total pressure and total temperature boundary conditions are specified in accordance with conditions of the CIAM experiment, NPR = 1.68 and $T_0 = 505$ K.

The geometry of the square nozzle including the downstream embodiment, which includes a deck merged with the bottom side of the nozzle lip and two triangular side walls is shown in Fig. 1. The height of the nozzle, h is 0.0566 m, the distance between the side walls, w is 0.127 m, and the deck length, $(x_1 - x_0)$ is 0.29 m, where the origin of the coordinate system is set to $x_0 = 0$.

For flow and turbulence modelling of the CIAM experiment, the zonal Unsteady RANS-LES (URANS-LES) approach [28] was implemented. Within this hybrid modelling framework, the nozzle interior together with an upstream part of the jet shear layers and the boundary layer region of the deck and the side walls are modelled by URANS, whereas the rest of the flow is modelled by LES. The coupling between RANS and LES was achieved using the Improved DDES (IDDES) method [32], which is based on the ideas of the integration of DDES [33] with another hybrid RANS–LES model intended for Wall Modelled LES. In the framework of the zonal RANS–IDDES approach, the RANS Spalart–Allmaras (SA) model [34] was implemented. Following [28], the synthetic turbulence generator with a three-dimensional source is used at the entrance to the IDDES subdomain to generate turbulent velocity fluctuations.

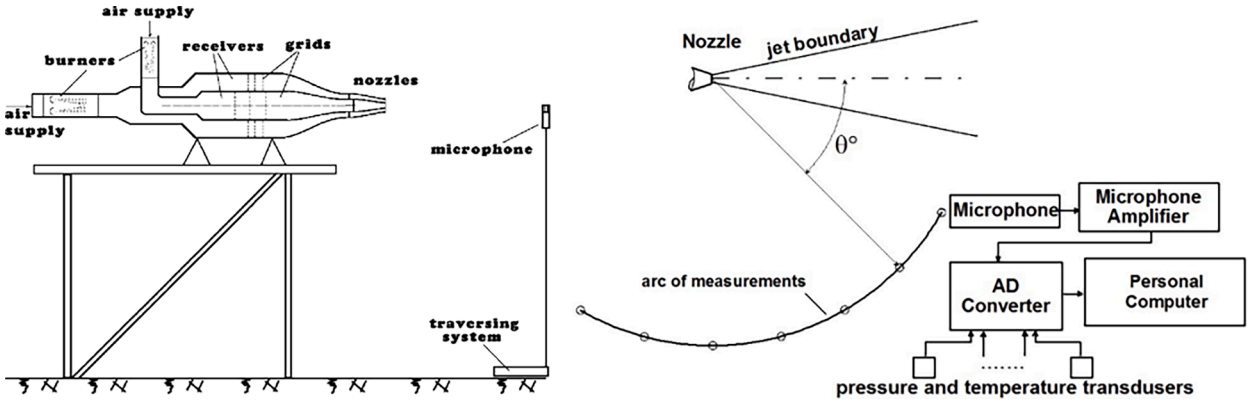

Fig. 2. Schematic of acoustic measurements in the CIAM facility.

The kinetic energy k of turbulent fluctuations missing in the SA model, which is required for calculating the source is determined using the Bradshaw hypothesis. The latter hypothesis relates the turbulent kinetic energy with the shear stress τ in accordance with an empirical linear proportionality law, $k = \tau/(\rho\sqrt{C_\mu})$, where ρ is density and C_μ is the empirical constant of the k-ε turbulence model. The implemented synthetic turbulence generator allows for a smooth emulation of unsteady velocity fluctuations upstream of the LES domain without generating spurious acoustic waves.

The numerical algorithm of the zonal LES solver is based on solving the governing Navier-Stokes equations using the fourth-order flux variable reconstruction MP5 scheme [35] combined with the Roe flux-splitting in each direction of the structured multi-block grid. The flux reconstruction uses a weighted combination of the central and upwind-biased approximations to ensure a trade-off between stability and low dissipation of the numerical solution. All viscous terms are discretized using second-order central differences. For time integration, a third-order implicit Runge–Kutta scheme is used, where the Adams formula is implemented to linearize the solution at the new time level, thereby avoiding the need for sub-iterations.

Two setups of the implemented IDDES model of the CIAM experiment are considered, which correspond to different locations of the synthetic turbulence generator, as a trade-off between the computational cost and fidelity of the resulting flow solution. In the first zonal URANS-LES setup (Figs. 3a, 4a), the entire jet flow upstream of the nozzle and above the deck wall is solved with a URANS model, so the location of the URANS-LES hybrid zone corresponds to the trailing edge of the deck ($x = x_1$). The URANS part of the model is aimed to capture the large-scale unsteadiness in the channel flow formed between the side walls of the jet embodiment from the upper nozzle lip to the deck trailing edge as well as the fine-scale turbulence. However, the URANS solution cannot correctly represent the large-scale coherent structures formed in the free-shear part of the jet flow above the deck, which is solved by LES. The broadband part of the flow is only resolved for the wake downstream of the deck trailing edge in this model. The motivation for this setup is that, since the URANS grid in the stream-wise and span-wise directions can be much coarser than LES, the total grid count of the URANS-LES model setup 1 is only about 20 million cells. Yet, the model should still capture the large-scale unsteadiness typical of the dominant low-frequency tone of the acoustic-flow resonance, assuming a scale separation between the tone and the turbulent fluctuations. In the second URANS-LES setup (Figs. 3b, 4b), the configuration of the URANS-LES region near the wall regions is kept the same as in the first setup. At the same time, the hybrid URANS-LES region above the deck was moved upstream and set at a distance of 0.4 ($x_2 - x_1$) from the upper nozzle lip, which is approximately equivalent to one effective rectangular nozzle diameter, D_j. Hence, in comparison with the first setup, the second model resolves most of the jet shear layer above the deck, whilst reducing to URANS to represent the initial shear layer downstream of the nozzle exit, thereby reducing the computational cost significantly in comparison with directly resolving small turbulent scales in this region like in pure LES. Because of the LES grid resolution requirements in the streamwise- and wall-normal grid directions for modelling of the jet shear layer development above deck, the total grid count of the second URANS-LES setup has increased to 60 million cells.

For all URANS-LES interfaces near the deck and the side walls, the stream-wise and tangential grid spacings were set to δ/5 and δ/6, respectively, where δ is the local boundary layer thickness. In the wall-normal direction, the grid spacing was varied from δ/42 near the wall to δ/6 in the outer boundary layer, where the grid cells were stretched with an increment of 1.1 in accordance with recommendations in the WMLES literature [26]. Further grid details of the two URANS/LES setups are shown in Fig. 5.

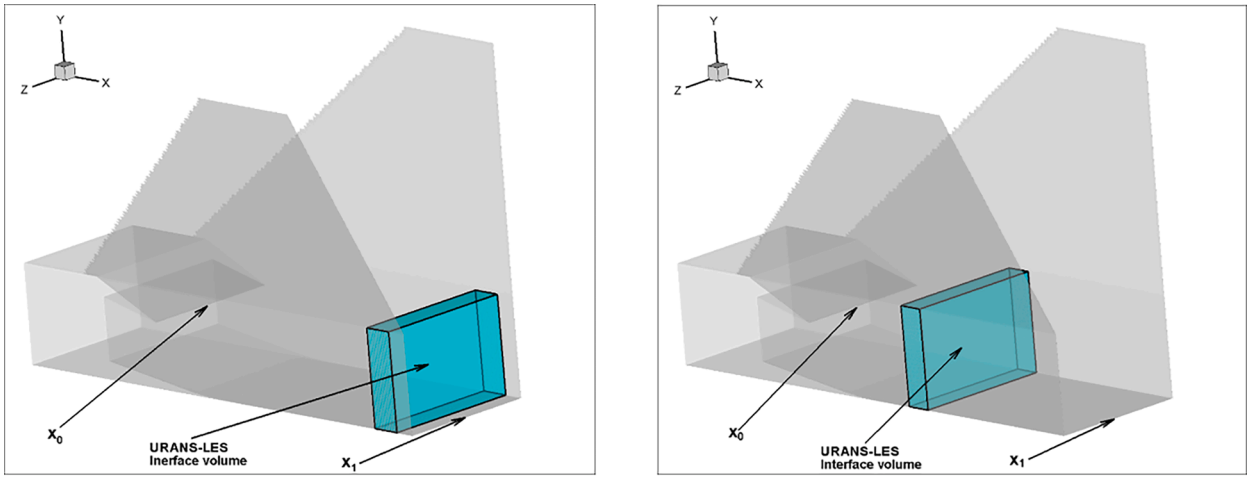

Fig. 3. Geometry and location of the URANS–LES Interface zone of setup 1 (a) and setup 2 (b).

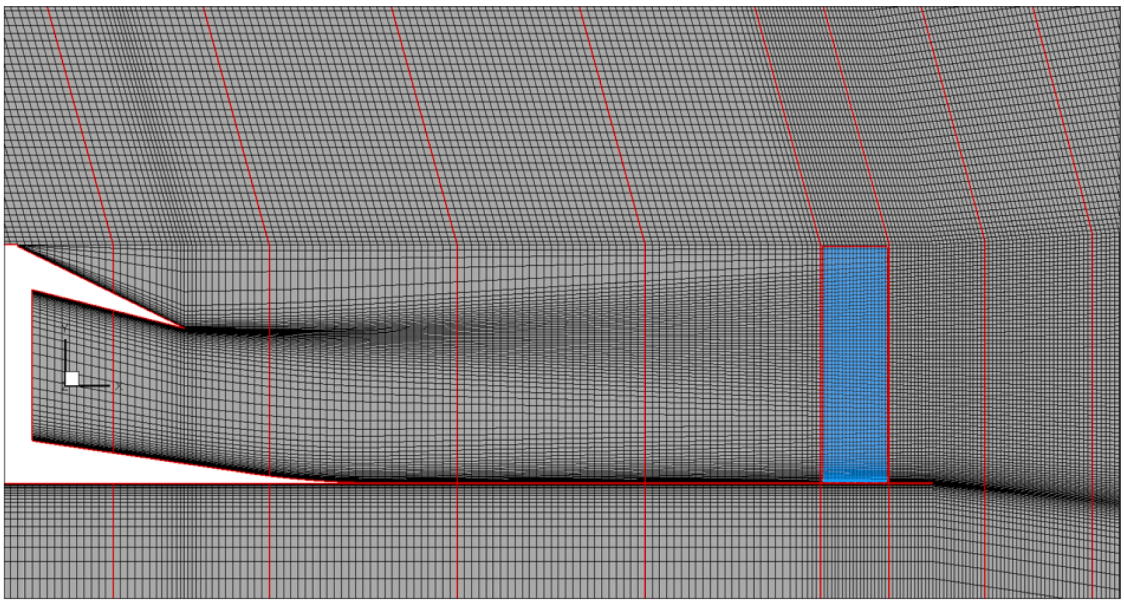

(a)

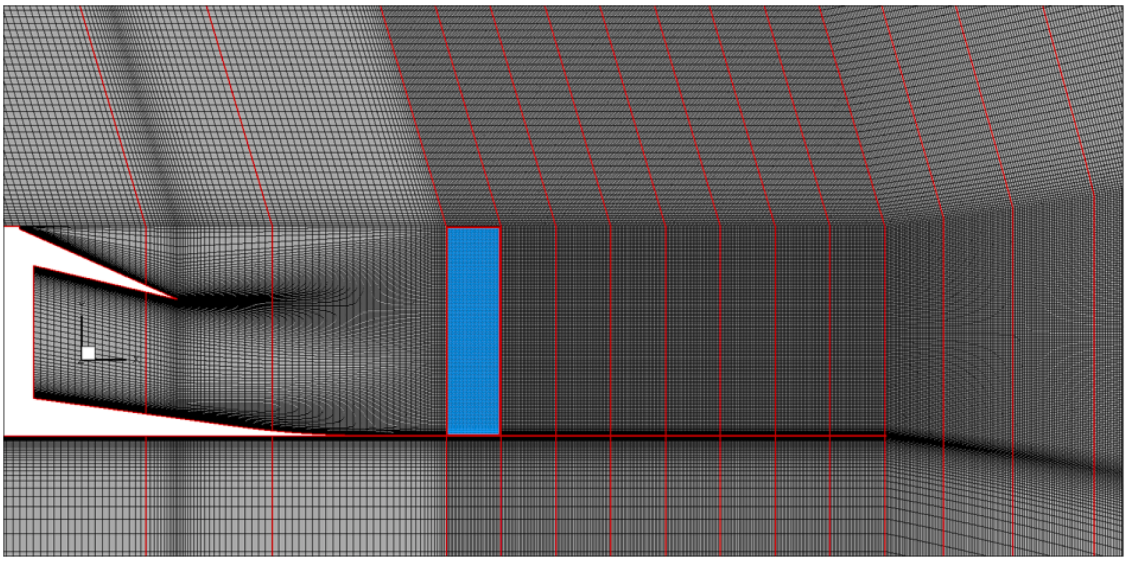

(b)

Fig. 4. Computational grids in the symmetry plan for the URANS-LES model setup 1 (a) and setup 2 (b) in the symmetry plane. The hybrid URANS-LES zone is shown as a rectangular box, and the pure LES region starts downstream of the box zone in each case.

3. Flow resonance in the baseline installed rectangular jet configuration

3.1. Cold versus hot flow analysis and model verification results

The flow solutions of setups 1 and 2 of the URANS-LES model are first obtained for an unheated jet issuing from the same installed rectangular nozzle at a total temperature of 288.15 K and the same ambient pressure, temperature, and acoustic Mach number conditions as in the heated jet CIAM experiment.

For consistency check of the two zonal LES setups, Fig. 6 shows vertical profiles of the turbulent kinetic energy and turbulent length scale at the upper nozzle lip and a further downstream axial location in the divergent part of the nozzle. The peaks of the turbulent

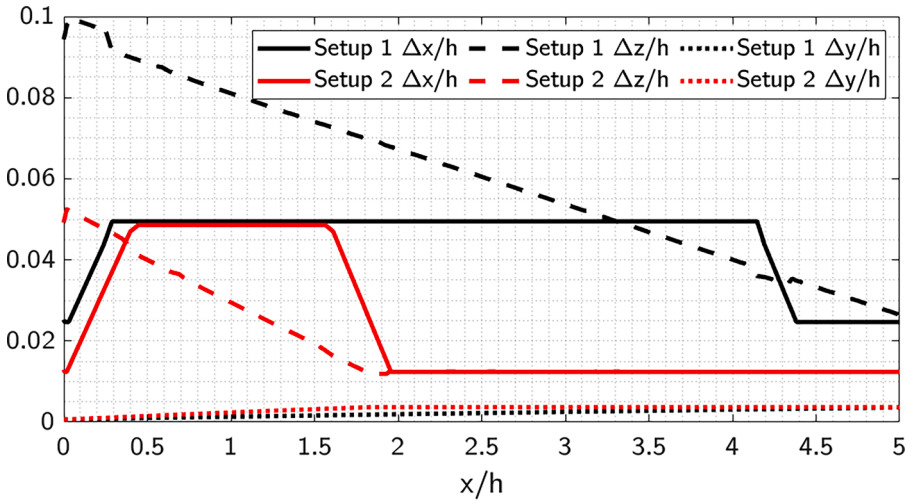

Fig. 5. Symmetry plane distributions of grid spacings on the deck wall normalised by the nozzle height, h for the URANS-LES setups 1 and 2.

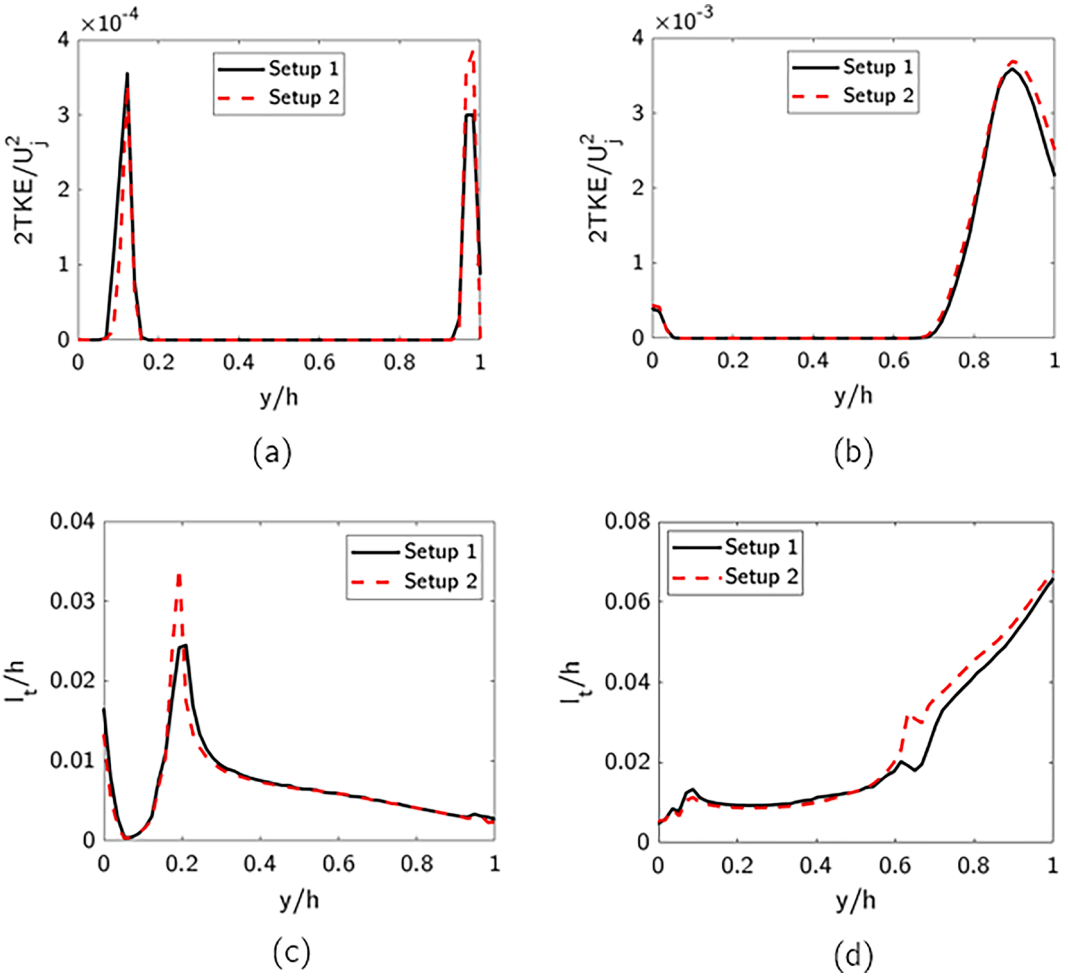

Fig. 6. Profiles of the turbulent kinetic energy at $x = 0$ (a), $x = 1.77\ h$ (b), and the turbulent length scale at $x = 0$ (c), $x = 1.77h$ (d) for the URANS-LES set-ups 1 and 2, where $y = 0$ corresponds to the bottom wall and $x = 0$ corresponds to the top lip of the nozzle.

kinetic energy corresponding to the bottom wall boundary layer and the nozzle lip are clearly visible in both cases in the nozzle exit profiles. The peak of the turbulent length scale corresponding to the wall boundary layer in the nozzle exit plane is also pronounced. For the downstream location, the broadening of the peaks of the radial distributions at the jet lipline location, as well as a rapid mixing of the wall boundary layer are well represented in accordance with the diverging behavior of the semi- bounded jet flow. Notably, good agreement in both the turbulent kinetic energy and the integral scale distributions demonstrated for two axal jet locations corresponding to the jet initial shear layer shows that turbulent inflow conditions of the two installed jet model setups have been matched consistently.

In both simulations, starting from the initial steady solution state, resonance-type oscillations develop in the jet after a relatively short transient period. The oscillations are quasi-periodic corresponding to a fundamental oscillation frequency of 580 Hz. Fig. 7 shows instantaneous snapshots of the pressure and Mach number distributions, corresponding to typical phases of the oscillation cycle with a large-scale wave propagating along the flapping jet shear layer obtained for setup 1.

Fig. 8 shows instantaneous snapshots of the Mach number and static pressure obtained from the two setups at the same phase of the oscillation cycle. Despite some differences in fine-scale flow structures above the deck at $x = 0.1 - 0.25$ m, where the URANS part of the solution of setup 1 looks like a time-averaged LES solution of the jet in setup 2, the dominant large-scale flow patterns reproduced by the two setups are very similar.

The large-scale flow oscillations obtained from the two zonal LES models are first compared by computing the integral lift force in the positive y-axis direction exerted on the entire installed nozzle structure, including the side walls and the deck. Fig. 9 shows the resulting lift forces produced by the two models, which are fairly similar in terms of the amplitude, frequency, and phase, once the solution reaches a resonance cycle after initial transients. This suggests that the dominant feature of the acoustic-flow resonance cycle has been consistently captured by both models, thereby indicating that the URANS modelling of the jet flow above the deck is sufficient to correctly represent the dominant low-frequency cycle at $f_0 = 580$ Hz.

To further analyze the spatial structure of the two solutions at the resonance frequency, $f_0 = 580$ Hz, the pressure and Mach number distributions in the jet symmetry plane are Fourier time-transformed at the same fundamental oscillation frequency. Figs. 10a and b compare the resulting spatial distribution of the Fourier amplitude of the setup 1 and 2 models. In each case, the numerical Fourier transform corresponds to solution averaging over 18 periods of the main tone. Fig. 10c shows a comparison of the Fourier amplitude distributions along the jet lipline, which are in very good agreement with each other.

In addition to the Fourier analysis, the pressure solutions of the two zonal setups have also been analyzed using Proper Orthogonal Decomposition (POD), using the snap-shot POD tool provided in [36]. In comparison with the Fourier analysis, POD automatically decomposes the turbulent flow field into modes from the highest to the lowest fluctuation energy without any need for the specific oscillation frequency input.

Figs. 11a-h show distributions of the magnitude of the first four leading spatial POD modes corresponding to the URANS-LES setups 1 and 2 in the jet symmetry plane. For quantitative comparison, Fig. 11i shows distributions of the dominant first POD mode along the jet lipline for the same two models. Again, the solutions of the two setups of the URANS-LES model are in very good agreement, thereby reconfirming that the large-scale dynamics of the jet resonance cycle is well captured regardless of the location of the hybrid zone region.

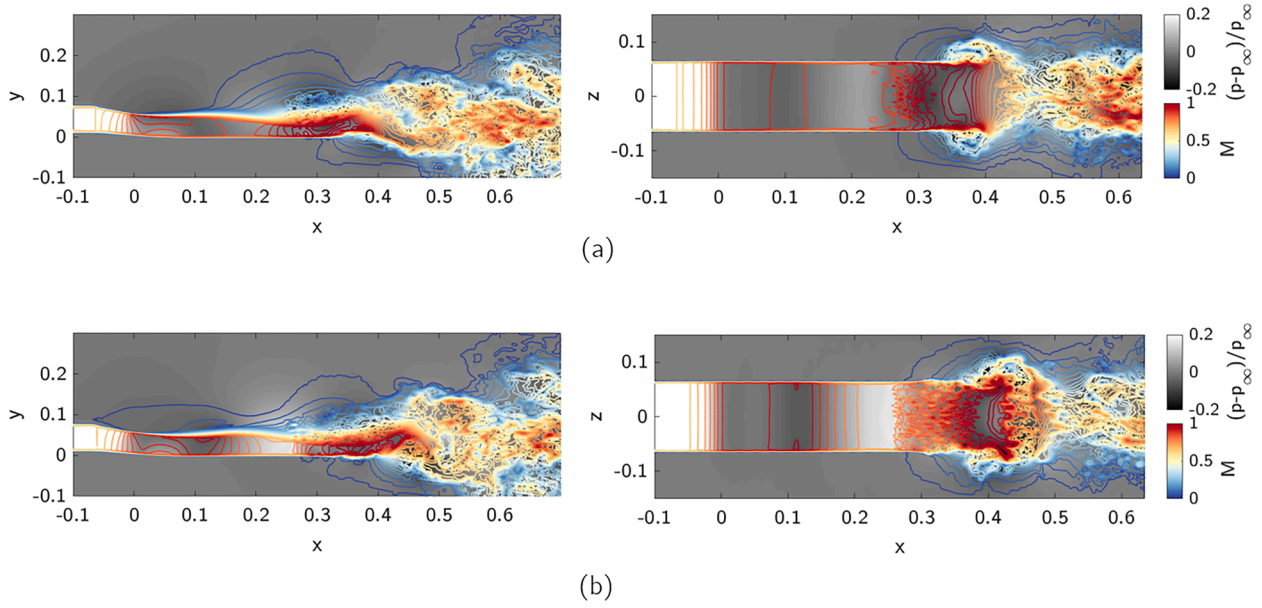

Fig. 7. Contours of the Mach number and static pressure, $(p - p_\infty)/p_\infty$ distributions in the vertical (left) and horizontal (right) symmetry planes at two consecutive phases of the flow resonance cycle shown in (a) and (b). The calculation corresponds to the URANS-LES model setup 1, and $x = 0$ stands for the edge of the upper nozzle lip.

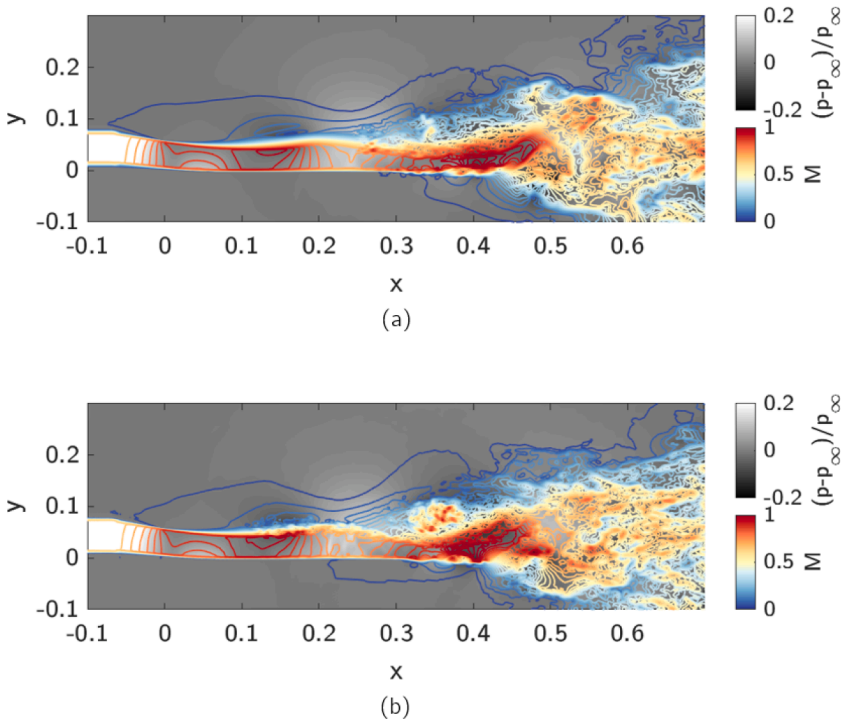

Fig. 8. Instantaneous distributions of the Mach number and static pressure, $(p-p_\infty)/p_\infty$ in the symmetry plane for setups 1 (a) and 2 (b) at the same characteristic time moment of the oscillating cycle. The hybrid URANS-LES zone is shown as a rectangular box in each case. $x = 0$ corresponds to the edge of the upper nozzle lip.

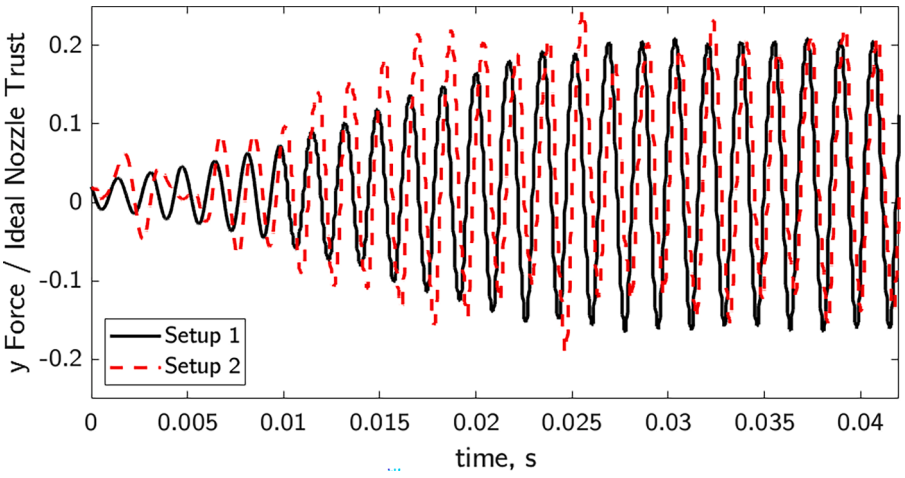

Fig. 9. Sensitivity of the URANS/LES model to resolving large eddies in the jet flow above the deck: the lift force on the installed rectangular nozzle corresponding to the solutions of setups 1 (pure URANS model of the semi-closed jet above the deck) and 2 (most part of the jet is modeled via LES).

3.2. Effect of the jet temperature on the flow resonance

Having verified that the oscillating flow solution is not sensitive to numerical parameters of the hybrid URANS-LES method, we can proceed with the investigation of the physical mechanisms, which cause the resonance. For example, one of the pertinent parameters of the acoustic-flow interaction is sound speed, which depends on the jet temperature. It can also be recalled that the CIAM experiment corresponded to a heated jet condition upstream of the nozzle at a total temperature of 505 K. Hence, for comparison with the simulations for the unheated jet, the heated jet calculation for the conditions of the CIAM experiment was performed for the zonal LES setup 2.

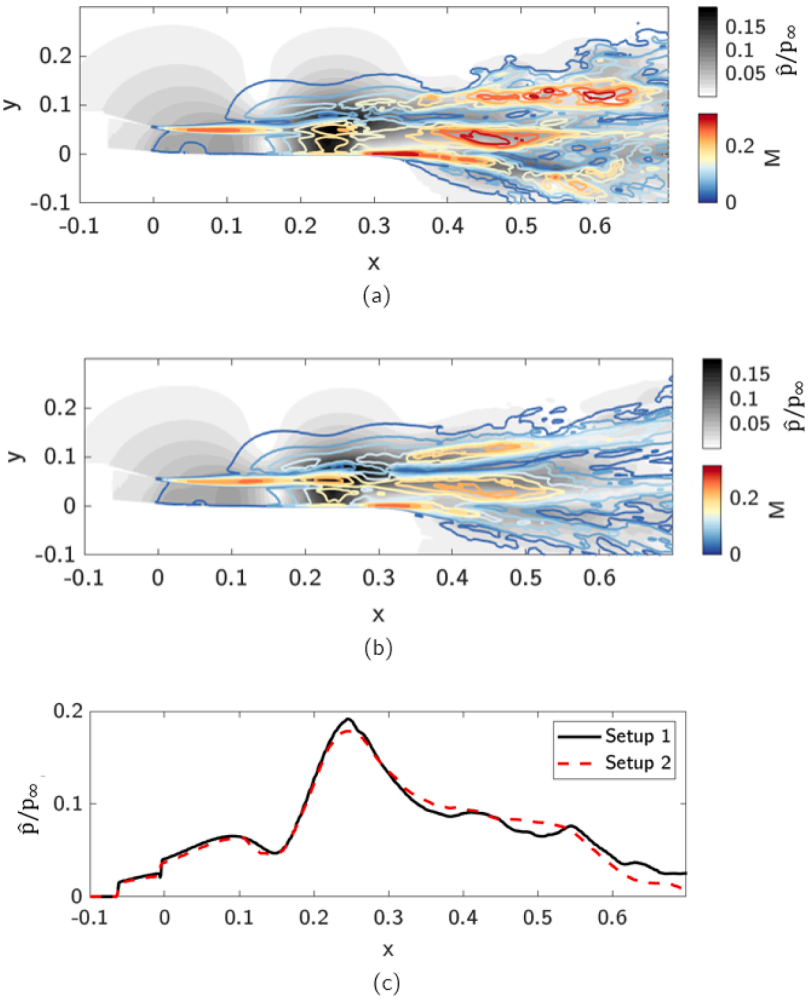

Fig. 10. Spatial distributions of the Fourier amplitudes and the Mach number fields in the symmetry plane corresponding to the fundamental frequency as obtained for URANS/LES setups 1 (a) and 2 (b). The comparison of the Fourier amplitude profiles along the jet lipline are shown in (c), $x = 0$ corresponds to the edge of the upper nozzle lip.

The simulation results of the heated jet model also show the resonance-type flow, whose fundamental frequency has increased from, $f_0 = 580$ Hz to 645 Hz. Notably, the frequency increase is less than that following from the Helmholtz number scaling, $\frac{f_{\text{heated}} \cdot D_j / \sqrt{\kappa \cdot R \cdot T_{\text{heated}}}}{f_{\text{unheated}} \cdot D_j / \sqrt{\kappa \cdot R \cdot T_{\text{unheated}}}} \approx 0.84$, thereby suggesting that the jet flow oscillations in question are caused by a coupling of acoustic and hydrodynamic effects.

To analyze the difference between the two jets further, Fig. 12 compares pressure power spectrum densities corresponding to locations of the maximum pressure fluctuation in the unheated and the heated jet flow. It can be noted that in both jet cases the pressure spectrum follows the same trend. The main tones are amplified by about 10 dB in comparison with the secondary tones and have similar amplitudes in the unheated and the heated jet solution. In addition, between the two jets, the multiples of the main tone are offset in frequency approximately proportionally to the ratio of the main tone frequencies multiplied by the multiple number. Altogether, this suggests that the tones in the unheated and the heated installed rectangular jet case are produced by a similar linear flow-acoustic wave interaction mechanism.

3.3. *Acoustic modelling*

For far-field noise spectra computation, the zonal LES solution of setup 2, which resolves most of the turbulent jet above the deck is combined with the frequency-domain FW-H method in the permeable control surface formulation [37-39]. Far-field noise solutions are obtained for both the heated and the unheated installed jet cases. A large FW-H integration surface of the rectangular funnel-type is used, which confines the rectangular jet and its embodiment. The control surface was extended sufficiently far in the jet downstream direction to contain all jet noise sources. The surface is open at the inlet and outlet sections to avoid any potential pseudo-sound effects

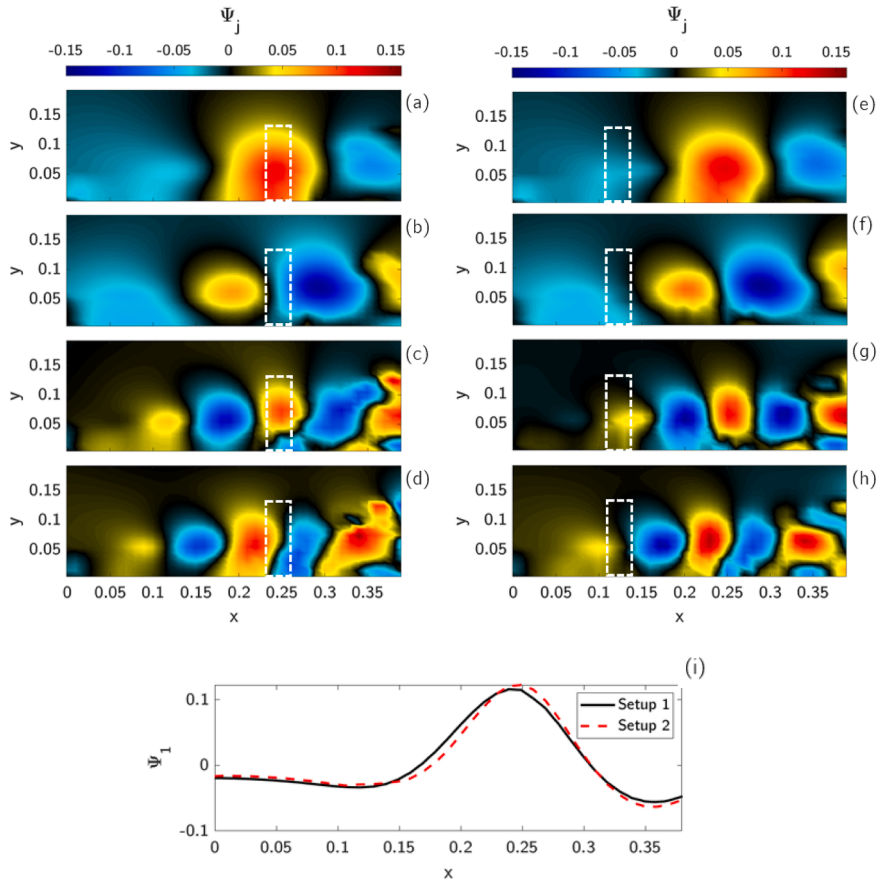

Fig. 11. Distributions of the magnitudes of the first four dominant POD modes of pressure fluctuations, Ψ_j, obtained in the jet symmetry plane for URANS/LES setup 1 (a,b,c,d) and setup 2 (e,f,g,h), where the POD mode numbers, $j = 1,2,3$, and 4 correspond to rows (a,e), (b,f), (c,g), and (d,h), respectively. The hybrid URANS-LES zone is shown as a rectangular box in each case. (i) compares the lipline distributions of the dominant mode for both URANS-LES setups.

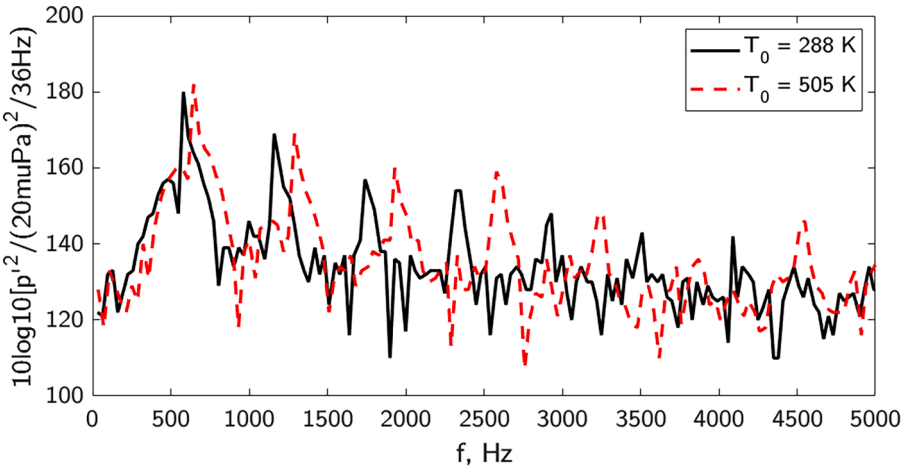

Fig. 12. Comparison of the pressure spectra computed in locations corresponding to the maximum fluctuation amplitude in the heated and the unheated jet. The main tone frequency of the unheated and the heated jet is 580 Hz and 645 Hz, respectively.

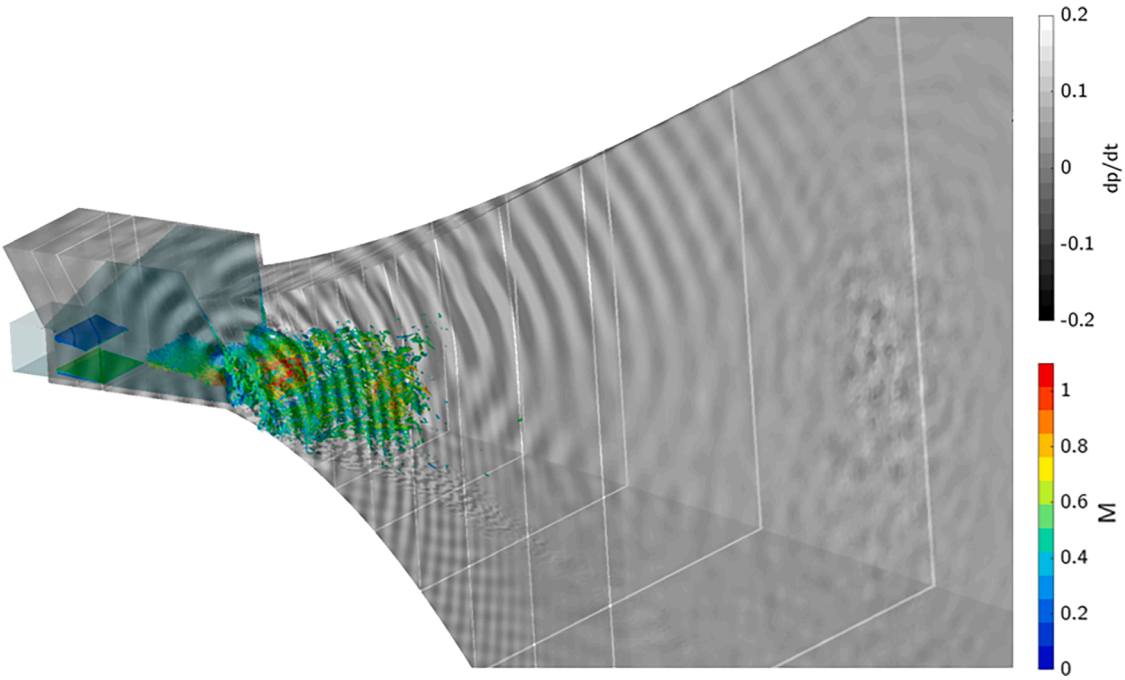

Fig. 13. Combining the zonal LES solution with the FW-H integral surface method: distributions of the instantaneous Mach number in the jet and the time derivative of static pressure inside the open control surface.

due to the FW-H surface crossing by vorticity waves. The solution of the zonal LES method used for the FW-H calculations, which was obtained after the initial spinout time, corresponds to 181 convective time units. The latter units are based on the effective nozzle diameter D_j and the jet velocity, U_j at the nozzle exit, $x = x_0$. Fig. 13 illustrates the position of the FW-H acoustic surface, which is placed well outside of the high-speed flow region for the heated jet LES case.

To assess the experimental uncertainty due to reflections in the non-anechoic CIAM aeroacoustic facility, noise measurements in the CIAM facility for an isolated round jet are cross-validated in comparison with the NASA SHJAR database. Fig. 14 shows the far-field pressure power spectra density measured for the reference round isolated jet in the CIAM facility by replacing the rectangular nozzle (see Section 2) with an equivalent isolated round nozzle. The noise measurements are compared with the consensus dataset from the NASA SHJAR experiment, which is represented by the sJet model based on the empirical scaling laws. Predictions of the sJet model correspond to the same upstream total pressure and temperature conditions as in the CIAM experiment. In both cases, the dependency of the far-field pressure power spectra density on Strouhal number, $\mathrm{St} = fD_j/U_j$ is shown. The reference sampling frequency corresponds to $\mathrm{St} = 1$, and the standard reference pressure, $p_{\mathrm{ref}} = 20\mu$Pa is used. Overall, it can be noted that the two datasets are in good agreement with each other for mid-high frequencies including the peak spectra for observer angles 45° and 60°. At the same time, some larger discrepancies are noticed for lower frequencies. The latter discrepancies are especially noticeable for 30° and 90° observer angles, where noise levels at the peak frequency of $\mathrm{St} \sim 0.2$ between the sJet dataset and the mean trendline fitted to the CIAM data for each observer angle differ by 3–4 dB In addition, the Fig. 14e,f,g,h shows the absolute deviations of the CIAM spectra from the corresponding means, which characterises the scatter in the experimental spectra. By interpreting the magnitude of the difference in noise levels between the mean trendline of the CIAM data and the sJet solution, σ_{mean} as well as the scatter of the CIAM data from the corresponding means, $\sigma_{\mathrm{scatter}}$ as statistically independent uncertainties, the total experimental uncertainty of the CIAM experimental facility for the round jet case is evaluated as $\sigma_{\mathrm{total}} = \sqrt{\sigma^2_{\mathrm{mean}} + \sigma^2_{\mathrm{scatter}}}$. The resulting σ_{total} is then used as the experimental error bar when comparing numerical predictions from the zonal LES model with the CIAM noise measurements for the installed heated rectangular jet flow case in Fig. 15.

Because of the relatively short LES signal available for statistical averaging of the complex broadband-tonal signal of the installed rectangular jet (181 convective time units, whereas 800–1000 convective units are recommended in state-of-the art jet LES for acoustic postprocessing to capture low frequencies [13,14]), the broadband component of the LES signal was computed separately from the tones. The separation of the broadband component was achieved by removing the first nine major tones from the original LES signal using the Fourier transform with a time window adjusted for each tone period. The resulting broadband time series for each observer angle were Fourier transformed using the multi-window Welch averaging method with a 50 % interval overlap to reduce statistical noise. It can be noted that the applied separation procedure used the standard assumption that the tonal and the broadband components of noise signals are uncorrelated.

Fig. 15 compares the broadband component of the noise spectra solution obtained from the zonal LES-FW-H method with the CIAM experiment. For all observer angles, the broadband part of the noise spectra is well captured within the experimental uncertainty up to

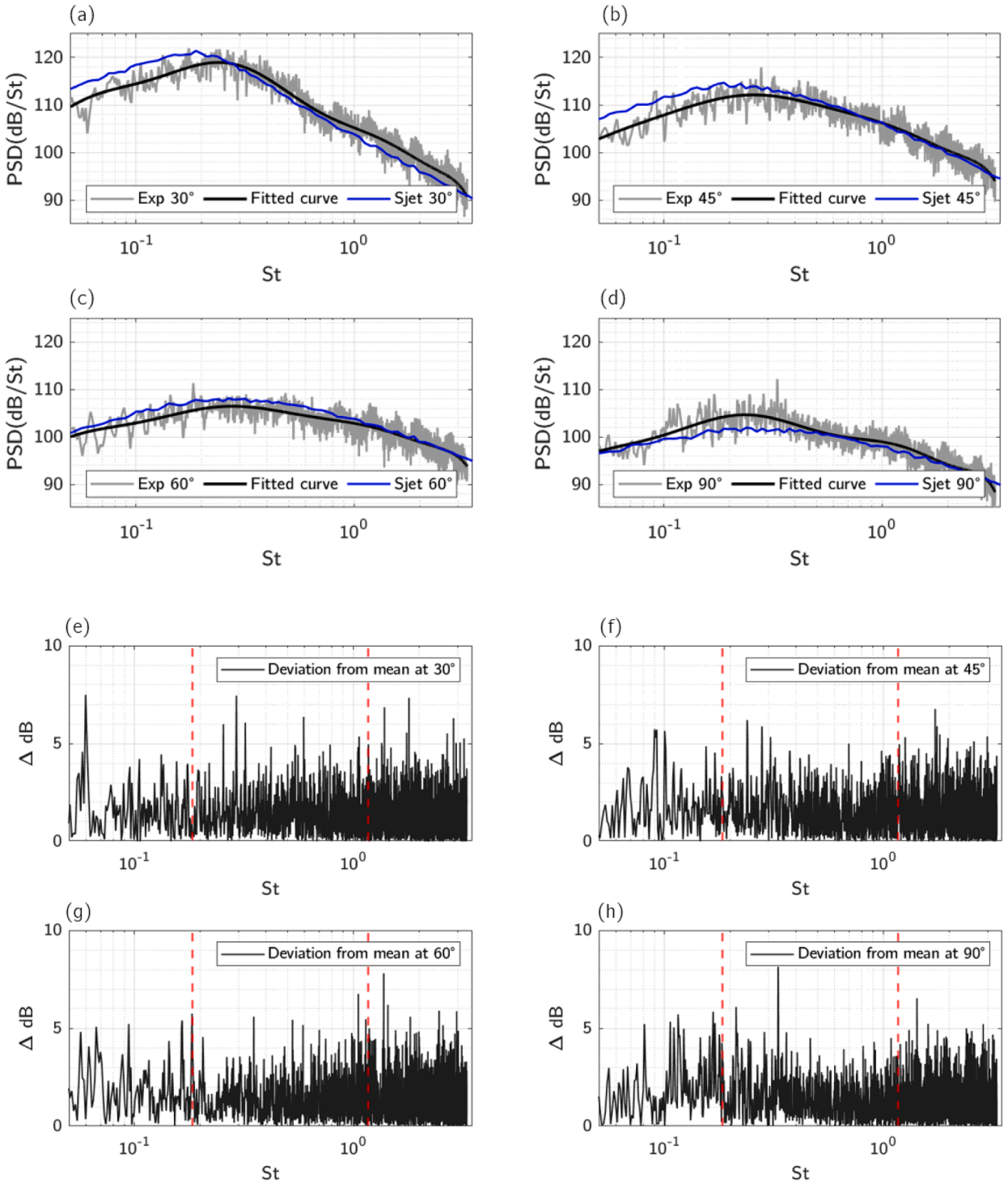

Fig. 14. Comparison of the reference isolated round jet measurements in the CIAM facility with the sJet model predictions representing the NASA SHJAR dataset for the same upstream jet conditions for observer angles: 30° (a), 45° (b), 60° (c), and 90° (d), where the mean trendline of the CIAM dataset is denoted by solid line. Absolute deviations of the CIAM spectra for each angle and frequencies, which characterise the scatter in the CIAM data are shown in (e),(f),(g), and (h), where vertical red dashed lines correspond to the first and the sixth harmonic of the main tone. The computed difference between the mean trendline of the CIAM dataset and the NASA data as well as the scatter in the CIAM spectra are treated as independent uncertainties of the CIAM measurement to calculate the total experimental error bar included in Fig. 15.

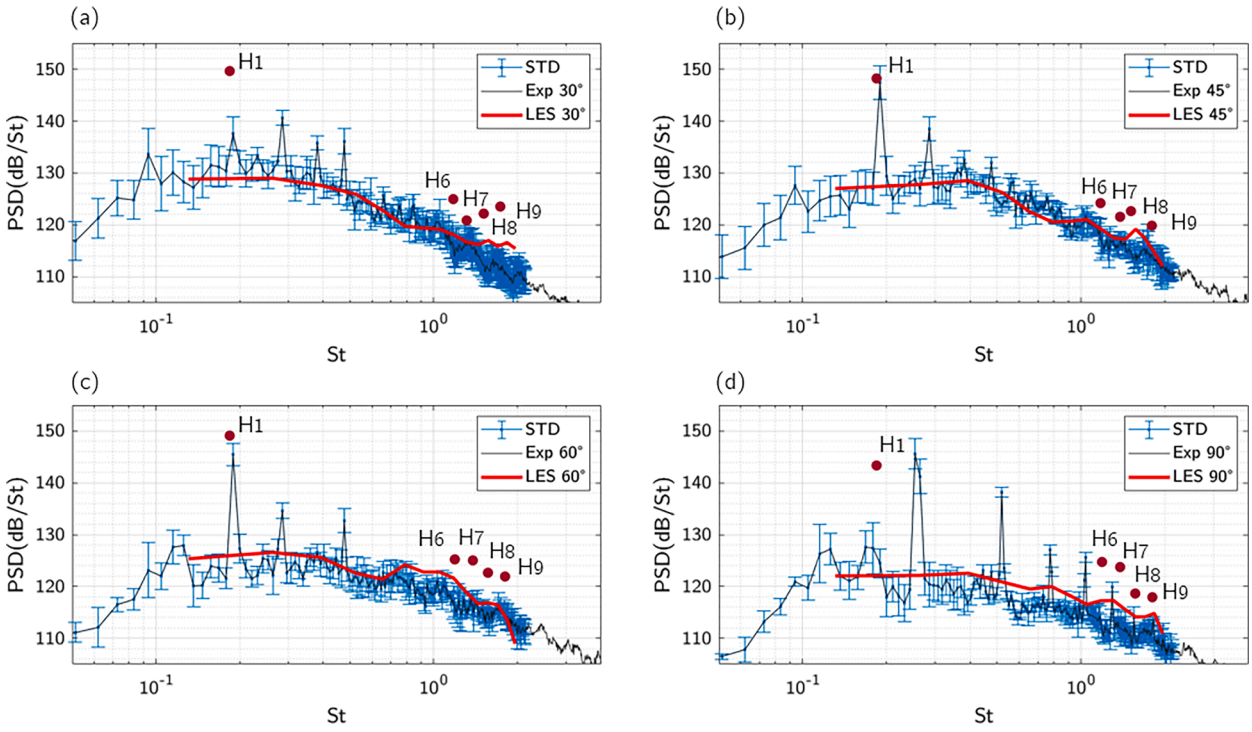

Fig. 15. Far-field noise predictions of the zonal LES- FW-H method in comparison with the CIAM measurements for observer angles of 30° (a), 45° (b), 60° (c), and 90° (d). Symbols correspond to the main tone predictions and the solid lines stand for predictions of the rest of the acoustic spectrum, which was treated as broadband. Error bars correspond to uncertainty previously evaluated by comparing the CIAM measurements for the isolated round jet case with the NASA data.

the frequencies corresponding to St $\sim$ 2. The main tone frequency and the amplitude are more-or-less within the error bar of the CIAM experimental dataset for intermediate observer angles, 45° and 60°. In addition to the main tone, acoustic predictions for the 6 th and a few further multiples of the main tone are compared with the experiment to assess accuracy of the numerical solution at high frequencies, which are more amenable to statistical analysis of the short LES time series compared to the main tone. Notably, current predictions of the 6 th tone (St $\sim$ 1) for 30°, 45° and 90° agree with the experiment broadly within the error bar. At the same time, the agreement of the higher frequency tones with the experiment at the 60° observer angle is less good. The higher discrepancy here can be explained by a larger scatter of the CIAM dataset for this angle at frequencies in the vicinity of St $\sim$ 1 in comparison with other angles. In particular, the CIAM dataset shows a stronger scatter for the 60° angle, which reaches about 7 dB and exhibits a highly oscillatory behaviour depending on frequency around St $\sim$ 1 (Fig. 14 g). This suggests that the experimental error bar computed in Fig. 15 for this angle could be underestimated in this case at high frequencies.

It can also be noted that the agreement between the main tone prediction of the zonal LES model and the experiment is less good for 30° and 90° observer angles. In particular, it should be noted that the frequency of the main tone predicted by the zonal LES method for the 90° angle is the same as for all other angles, $f = 645$ Hz (St $\sim$ 0.2), consistently with the fundamental tone frequency of the flow solution (Fig. 11). However, the far-field noise measurements for this angle show a notable shift of the tone to a higher frequency. It can be argued that the shift of the main tone frequency in the CIAM noise dataset at 90° observer angle as well as the overprediction of the tone amplitude at 30° angle may be related to larger uncertainties of the CIAM measurements at low frequencies, which were detected for the pure broadband jet noise case (Fig. 14). Stronger reflections in the non-anechoic CIAM facility at these two angles at low frequencies may have a more pronounced effect on the acoustic tones in the installed rectangular jet in comparison with other observer angles.

3.4. Spectral and conditional analysis of the installed rectangular jet flow

Having validated the noise spectra solutions of the zonal LES method for the CIAM installed rectangular jet experiment using the URANS-LES setup 2, the unsteady jet flow solution is further analysed to understand mechanisms of the acoustic-flow resonance phenomenon.

First, the pressure fluctuations in the symmetry plane along the upper jet lip-line in the pure LES zone from a location downstream of the URANS/LES hybrid zone to the deck trailing edge are Fourier transformed in time and x-coordinate. While the acoustic wavelength of the main tone is too large to fit within the available Fourier transform domain, the length of the integration domain is sufficiently long to contain several acoustic wavelengths of the sixth multiple of the main tone and higher frequencies. The noise spectra corresponding to the sixth harmonic and some of the higher frequencies was found to be within a reasonable agreement with acoustic measurements as discussed in Section 3.3. It should be noted that, while the grid resolution in the vicinity of the FW-H surface for frequencies higher than the nineth multiple of the main tone was insufficient for far-field noise propagation, the LES solution inside the jet was well resolved to support acoustic wave propagation up to the frequencies corresponding to at least 60 multiples of the first tone.

Fig. 16 shows results of the Fourier transformation as a wave number - frequency diagram, from which a numerical dispersion relation of acoustic waves propagating in the installed rectangular jet is educed, obtaining the phase velocity for each frequency, $v_{\text{phase}}(\omega) = \omega/k$, $\omega = 2\pi f$. A notable feature of the $k-\omega$ diagram in Fig. 16a is horizontal lines corresponding to the strongly amplified pressure fluctuations at each multiple of the main tone frequency. The process of reconstruction of the numerical dispersion relation is illustrated in Fig. 16b, which shows the double peak of the Fourier amplitude distribution for each frequency corresponding to the two branches of the dispersion relation. The two branches are associated with the upstream and downstream propagating pressure waves in the jet above the deck. Fig. 16a shows that the phase velocity of the upstream wave tends to decay at high frequencies, thereby suggesting a certain cut-off for high-frequency acoustic waves propagating against the flow direction. In comparison with this, the downstream wave corresponds to a more-or-less constant slope of the dispersion relation, hence, always cut-on acoustic waves propagating in the flow direction. The similarity with the oblique wave propagation in a duct flow suggests that the pressure waves propagating upstream in the installed rectangular jet are also oblique. Furthermore, by computing the phase speed from the numerical dispersion relation, the axial distance, L, which separates the upstream and downstream reflection points in the jet to close the resonance loop can be estimated for each acoustic frequency. Indeed, the time taken by an acoustic wave to travel from the downstream reflection point to the upstream and back is $\frac{L}{|v_{\text{upstream}}|}+\frac{L}{v_{\text{downstream}}}$. Since this time also corresponds to the acoustic wave frequency, $1/f$, the distance is given by: $L = f^{-1}\frac{|v_{\text{upstream}}|\cdot v_{\text{downstream}}}{|v_{\text{upstream}}|+v_{\text{downstream}}}$.

Table 1 summarises the obtained phase values and axial distances for the 6 th and the 24 th multiple of the tone frequency. It can be recalled that the reason for choosing the smaller wavelengths in comparison with the fundamental tone is that, due to the limited LES

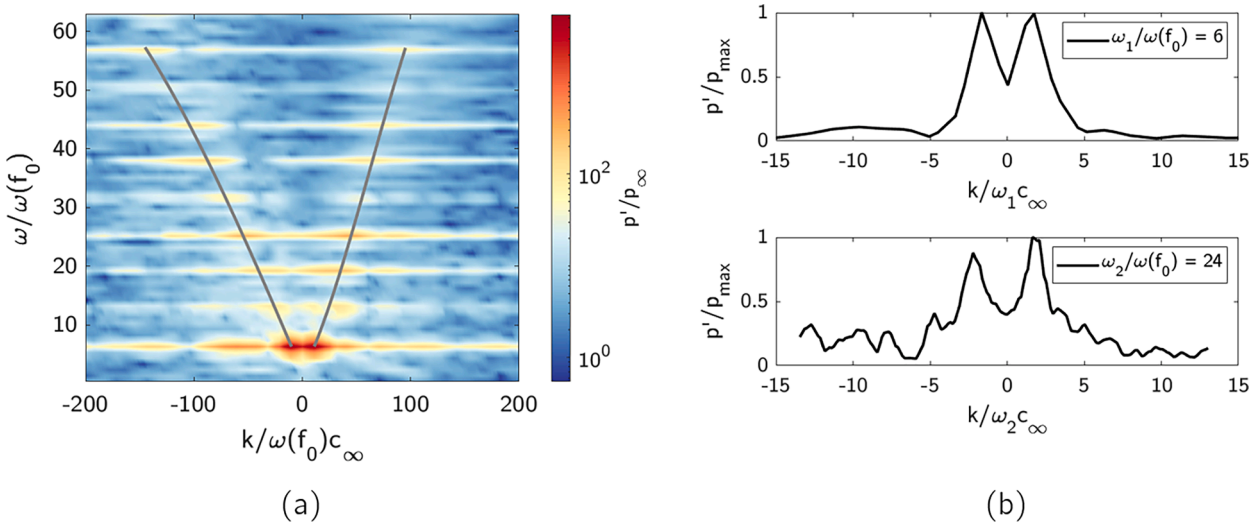

Fig. 16. Reconstruction of the numerical dispersion relation for pressure wave propagating in the installed rectangular jet using the zonal LES solution: wave number-frequency Fourier transform diagram for pressure fluctuations computed in the symmetry plane along the jet lipline location (a) and profiles of the pressure Fourier amplitudes at two multiple tone frequencies, $\omega_1/\omega(f_0) = 6$ (top) and $\omega_2/\omega(f_0) = 24$ (bottom), which illustrated the process of reconstruction of two branches of the numerical dispersion relation (b).

Table 1
Phase speed values and axial distances between the upstream and downstream reflection points in the jet for the 6 th and the 24 th multiple of the tone frequency.

	$\lvert v_{\text{upsteram}}\rvert$, m s^{-1}	$v_{\text{downstream}}$, m s^{-1}
$\omega_1/\omega(f_0) = 6$	213 $L = 0.0269$ m	203
$\omega_2/\omega(f_0) = 24$	157 $L = 0.0054$ m	180

domain in the streamwise direction available for the Fourier analysis, only the higher-order wavenumbers starting from the 6 th tone harmonic correspond a sufficiently small wavelength for accurate spectral analysis. The 24 th tone multiple is also included in the analysis to check and confirm the trend that, in accordance with the computed phase speeds and distances, the resonance loop in the considered installed rectangular jet does not occur between the deck trailing edge and the upstream nozzle lip (or an upstream receptive point in the early shear layer close to the nozzle lip) but, more likely, depends on internal reflection points located well inside the developing jet flow region. Furthermore, because the upstream-travelling pressure wave is oblique, as it follows from the educed numerical dispersion relation, internal reflection points may not be necessarily located in the same *x*-*z* or *x*-*y* plane, thereby indicating the presence of complex 3D wave reflections.

In can be noted that internal reflection points, such as those typical of trapped waves inside an isolated axi-symmetric jet flow can be analysed using a range of semi-analytical techniques [11]. However, extending such semi-analytical analysis tools to the 3D installed rectangular jet case represents a formidable challenge. Hence, in the current case, locations of the reflection points inside the installed rectangular jet will be analysed using a purely data-driven approach. Specifically, the Linear Stochastic Estimation (LSE) method will be used, which is also referred to as conditional averaging [40-42]. The idea of LSE is to de-noise spatial distributions of short time series using a correlation with control time signals, which are not contaminated by random turbulence. The implementation is briefly summarised as follows:

Several numerical probes in the linear hydrodynamic jet flow region (e.g. where the meanflow velocity becomes <2 % of U_j) are considered, where pressure measurements are taken, $q_i(t),\ i = 1,..,$ M. The computed pressure time signals in these numerical probes will be referred to as control signals. The probes are positioned in the jet symmetry plane at a distance of 2–3 h above the deck wall and aligned in the x-direction. For simplicity, the probes follow the LES grid lines, and their locations are selected as a trade-off between maintaining an acceptable numerical grid resolution for resolving acoustic waves and keeping away from the areas of significant vorticity in the jet flow (see Fig. A1, right). The latter is important to exclude any contamination of the control signals by the turbulent fluctuations, whose random behavior is not related to the acoustic-flow resonance mechanism.

At the initial step, to separate the effect of the frequency, instead of the full pressure fluctuation $p(\mathbf{x},t)$, contributions to pressure fluctuations at each frequency are computed,

$$p_\omega(\mathbf{x},t) = \frac{1}{2\pi} e^{i2\pi ft} \int p(\mathbf{x},t) e^{-i2\pi f\tau} d\tau. \tag{1}$$

In the framework of the LSE method, the pressure fluctuations in each point of the jet flow is presented the pressure flow field at each point of the turbulent jet flow, $\mathbf{x}$ as two parts: a correlated field, $p_\omega^{\mathrm{corr}}(\mathbf{x},t)$ and an uncorrelated field, ε with respect to the space of control signals:

$$p_\omega(\mathbf{x},t) = p_\omega^{\mathrm{corr}}(\mathbf{x},t) + \varepsilon, \tag{2}$$

where the correlated field can be represented by a linear expansion series linearly depending on control signals, q_i

$$p_\omega^{\mathrm{corr}}(\mathbf{x},t) = \sum_{i=1}^{M} \alpha_i(\mathbf{x}) q_i(t). \tag{3}$$

Assuming orthogonality of the control signals and the noise field, $\langle \varepsilon \cdot q_k(t) \rangle = 0$, the expansion coefficients $\alpha_i(\mathbf{x})$ are obtained from solving the linear system with $i,k = 1,..,M$, which follows from computing a scaler product between (1) and each control signal:

$$\langle p_\omega(\mathbf{x},t) q_k(t) \rangle = \sum_{i=1}^{M} \alpha_i(\mathbf{x}) < q_i(t) q_k(t) >, \tag{4}$$

so that

$$\begin{bmatrix} \alpha_1(\mathbf{x}) \\ \cdot \\ \alpha_M(\mathbf{x}) \end{bmatrix}^T = \begin{bmatrix} \langle p_\omega(\mathbf{x},t) q_1(t) \rangle \\ \cdot \\ \langle p_\omega(\mathbf{x},t) q_M(t) \rangle \end{bmatrix}^T \cdot \begin{bmatrix} < q_1(t) q_1(t) > & \cdot & < q_1(t) q_M(t) > \\ \cdot & \cdot & \cdot \\ < q_M(t) q_1(t) > & \cdot & < q_M(t) q_M(t) > \end{bmatrix}^{-1}. \tag{5}$$

In the above, the scalar product brackets mean time averaging, e.g.

$$\langle p_\omega(\mathbf{x},t) q_k(t) \rangle = T^{-1} \int_0^T p_\omega(\mathbf{x},t) q_k(t) dt, \tag{6}$$

wherein T stands for the time window of the LES dataset used for time averaging.

For the LSE flow analysis, the same arrays of control points in the symmetry plane above the jet is used to calculate the corresponding correlated pressure fields using (2) and (3) in two jet planes: (i) symmetry plane *x*-*y* and (ii) the horizontal plane *x*-*z* passing through the edges of the side walls of the jet embodiment.

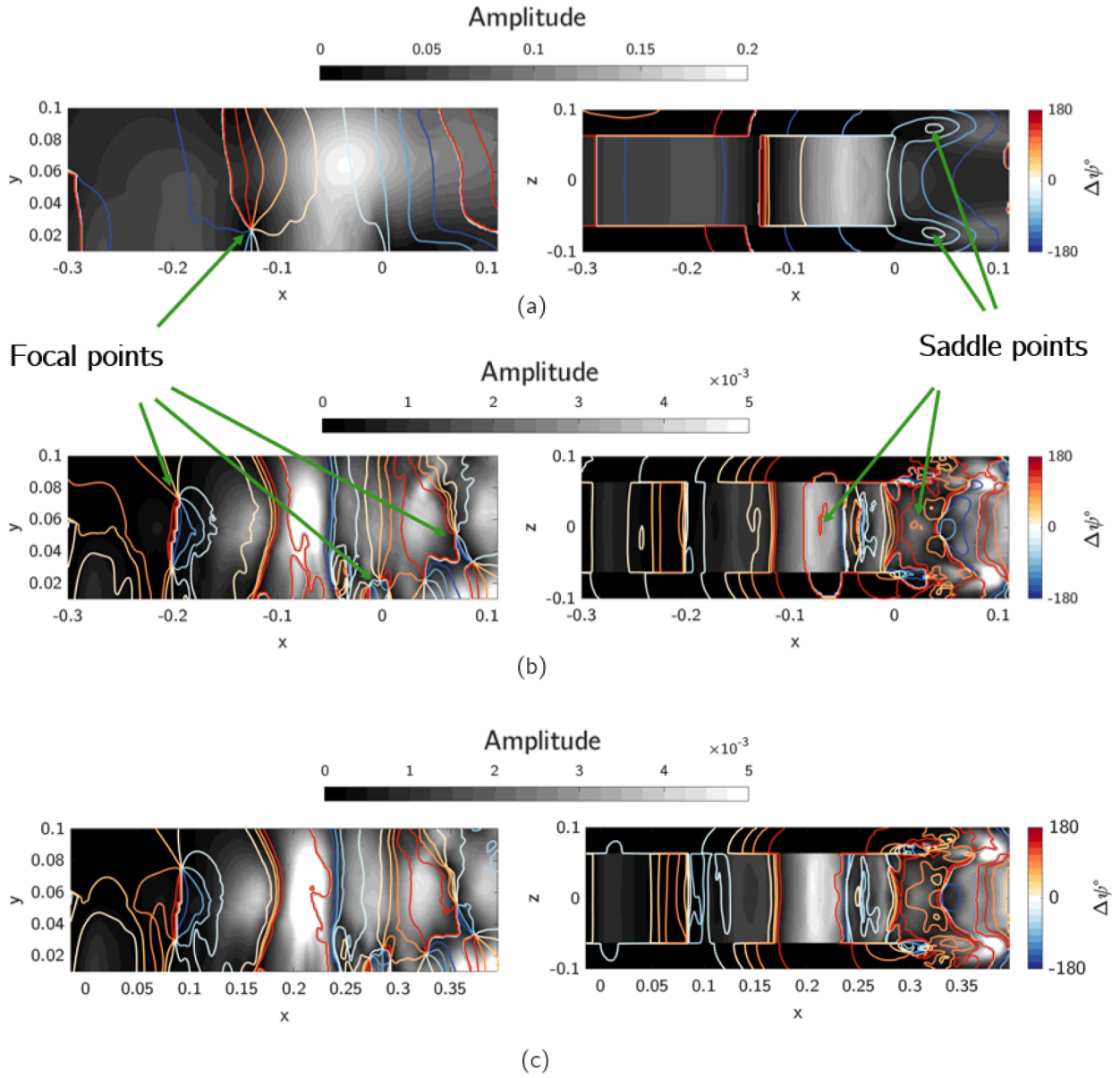

Fig. 17. Conditional averaging of pressure fluctuations of the installed rectangular jet: amplitude and phase distributions in the jet symmetry plane (left) and the same in the horizontal plane passing though the pointed edges of the side walls (right). (a) shows results for the main tone, (b) shows results for the sixth multiple of the main tone, and (c) shows LSE results for the sixth multiple harmonic using one-half of the control points q_i in comparison with the results of the full set in (b).

Fig. 17a shows the amplitude and the phase distributions of the conditionally averaged pressure field for the control pressure signals corresponding to the main tone frequency, f_0 in the jet symmetry plane (left) and the horizontal plane passing through the side wall edges (right). Fig. 17b shows the same fields for the sixth multiple of the main tone, $f = 6f_0$.

Patterns of the amplified pressure obtained from the LSE analysis visualize the spatial distribution of the part of the jet pressure fluctuations, which are correlated with the linear hydrodynamic pressure. The maxima of these distributions can be associated with the standing acoustic waves in the jet. At the same time, patterns of the phase obtained from LSE visualize the correlated pressure wave propagation in the jet. Notably, the phase fronts have a curved shape, indicating the complex three-dimensional nature of acoustic-flow resonances in the installed rectangular jet. Furthermore, certain features of the computed phase fronts can provide important insights into the fluid mechanics mechanisms of the acoustic-flow resonance. For example, the focal regions of abrupt phase changes by $\pm 180^o$, can be interpreted as wave reflection points inside the jet. Some of these points are clustered near the deck wall ($y \approx 0$) at $x \approx 0.15$ m, indicating the oblique wave reflections from the bottom wall (Fig. 17a left). The internal reflection patterns become more complex for the higher frequency case (Fig. 17b left), which shows multiple points of abrupt phase changes just upstream of the deck trailing edge at $x \approx 0.25$m and $x \approx 0.28$ m. Recalling that the trailing edge corresponds to $x = 0.29$ m, this manifestation of oblique wave reflections may explain the surprisingly small axial separation length between the upstream and the downstream reflection points from the stream-wise propagation dispersion analysis (Table 1).

In the high frequency case, strong reflections are also visible near the pointed edges of the side walls at $x \approx 0.29$ m and $z \approx \pm 0.06$ m (Fig. 17b right). From the x-z plane phase distributions (Fig. 17 right), it can also be noted that no appreciable reflection points occur near the lateral walls of the jet embodiment. In addition to the reflection points, the LSE results also include some saddle points, which are indicative of localised noise sources. For example, in the main tone case, two of such saddle points emerge downstream of the side wall edges at $x \approx 0.32$ m and $z \approx \pm 0.08$ m (Fig. 17a right). These points can be associated with the tip vortices shed from the pointed wall edges, which generate pressure waves coherently with the tone.

As a numerical sensitivity test, an additional LSE model setup was tested by considering an array of control points obtained by removing every other point from the original set of control points q_i along the jet flow.

Results of the LSE analysis for the sixth multiple of the main tone in the vertical (left) and the horizontal (right) plane are shown in Fig. 17c, which should be compared with the results for the full set of control points shown in fig17b. Notably, all major patterns identified earlier as reflection points in the installed rectangular jet remain virtually the same. This confirms that the implemented LSE-based identification procedure is sufficiently robust.

Collectively, the above results of the dispersion and LSE analyses suggest that the resonance cycle corresponds to oblique acoustic waves reflecting from the bottom wall and the edges of the side walls immersed in the upper shear layer of the jet, as shown schematically in Fig. 18. Notably, the reflection patterns of the considered installed rectangular jet are different in comparison with the canonical perfectly expanded jet flow above the flat plate, where upstream reflections could be associated with the receptive points in the early shear layers [10].

Following the obtained insights, in the next section, several modifications of the side wall edges of the CIAM installed rectangular nozzle geometry will be considered in attempt to break the acoustic-flow resonance cycle by removing the effect of the edges, thereby removing the tone.

4. Modification of the nozzle embodiment geometry to suppress the flow oscillations

4.1. Nozzle configurations tested and flow results obtained

To validate conclusions of the previous section, a series of additional zonal LES calculations of the heated installed rectangular jet

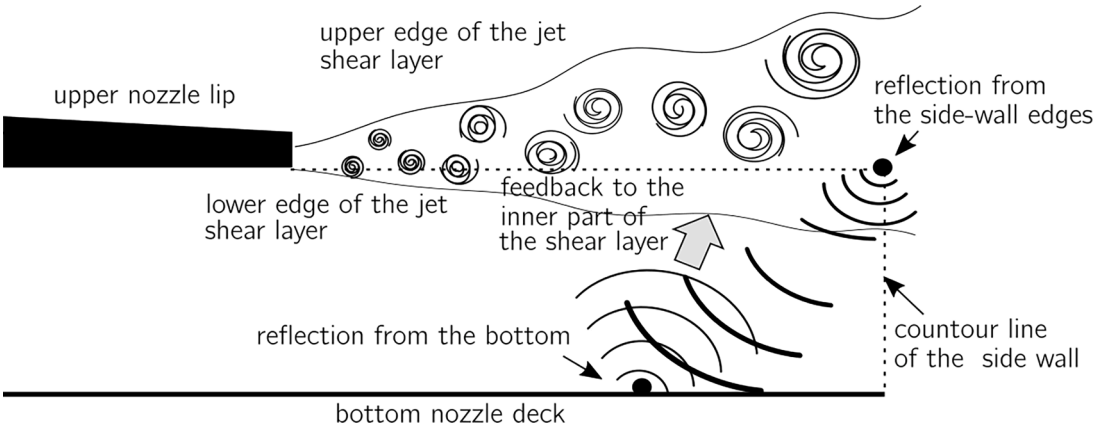

Fig. 18. Schematic of the flow-acoustic resonance mechanism in the installed rectangular jet.

has been performed. In all cases, the grid resolution has been kept the same as in the baseline URANS-LES setup 2, which simulates most part of the jet above the deck in the LES regime. The upstream nozzle geometry and boundary conditions have been kept the same, whilst several modifications have been applied to the downstream part of the deck and/or the side-wall geometry. The modifications correspond to 7 additional zonal LES calculations, whose results are summarised in Table 2. In each case, the left column shows the modified installed rectangular nozzle geometry, and the right column shows the resulting space-time distribution of the fluctuating pressure signature on the deck wall surface in the jet symmetry plane obtained from the zonal LES model.

The table starts with the results of the baseline case, which corresponds to a strong acoustic-flow resonance at the main tone frequency $f_0 = 645$ Hz. The first modification of the baseline case, labelled as configuration A was obtained by changing the rectangular trailing edge of the nozzle deck by modifying the reflection condition at the deck trailing edge using a serration. This modification was set to test if the main acoustic-flow resonance loop of the baseline installed rectangular test occurs in *x*-*z* plane between the deck trailing edge and some upstream point in the jet shear layer. For example, if changing the reflection condition at the deck trailing edge could change the tone, this would explain the resonance by the interaction of normal acoustic waves propagating in the *x*-direction. However, the tone in the modified configuration has remained virtually unaffected, hence, disproving the importance of the deck trailing edge for the resonance in the current case. Along the same line of thought, configuration B was to probe the importance of wave reflections from the two side edges of the lateral walls of the baseline geometry by introducing serrations there. Again, apart from some increase of the tone frequency, no appreciable change of acoustic-flow resonance was observed in this case either, thereby confirming conclusions of the analyses in the previous section that the observed resonance in the installed rectangular jet must be due to the out-of-plane oblique acoustic wave reflections, suggesting the importance of the side-wall corner points.

Hence, the next series of configurations, C, D, and E was to progressively smooth out the corners on the edges of the lateral walls by making the corresponding edges more oblique (C,D), or completely remove them by aligning the side edges with the triangular top elements (E). To separately analyze the side edge effect from the deck trailing edge, E keeps the baseline rectangular shape of the deck trailing edge. In comparison with configuration C, D was further used to investigate the pointed shape effect of the upper triangular part of the side walls. However, the latter effect was found to be negligible: both C and D produce very similar oscillating flow patterns, which only differ by a small shift of the tone frequency, whereas C also corresponds to some 10 % higher velocity of the flapping jet flow compared to D. Apart from the minor differences mentioned, configurations C and D reproduce the same acoustic-flow resonance as the baseline configuration (comp. Figs. 19a with Fig. 8b). At the same time, configuration E has been found successful in removing the tones from the wall pressure signal. Its flow solution reproduces a tone-less smoothly evolving jet (Fig. 19b), thereby confirming that fully removing the pointed edges of the side walls was essential for breaking the acoustic-flow resonance cycle of the CIAM configuration.

Having established the importance of the side-wall corner points on the acoustic-flow resonance, two additional configurations, F and G have been considered to separate this feature from the possible influence of the vertices of the triangular elements on the top. Hence, configuration F consists in removing the vertices of the triangular side walls from E. And the 'square-box' configuration G goes to the extreme of completely leveling off the triangular top parts of the side walls, whilst keeping the sharp side-wall edges of the baseline configuration. The results of testing configuration F show that the top vertices of the triangular wall have no apparent effect on triggering the acoustic-flow resonance. A possible explanation for this is that the tops of the triangular elements are outside

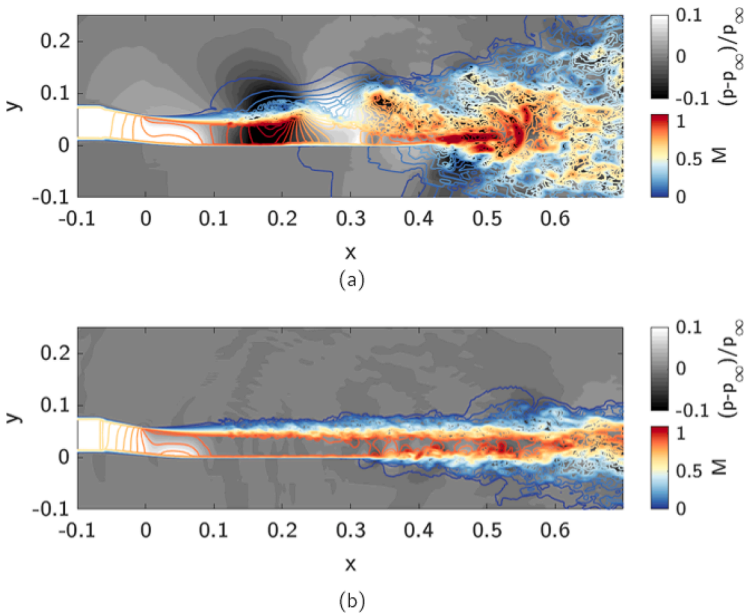

Fig. 19. Instantaneous Mach number and static pressure, $(p - p_\infty)/p_\infty$ distributions in the symmetry plane for configurations C (a) and E(b).

of either the jet shear layer or the linear hydrodynamic flow region near the end of the jet potential core, thereby their influence on the resonance is minimal. At the same time, the downstream edges of the side walls in configuration G play a crucial role in closing the acoustic/flow resonance cycle, thereby reproducing the tone again, albeit at somewhat higher frequency in comparison with the baseline case.

Table 2. Baseline and modified configurations of the installed rectangular nozzle vs. their resulting wall surface pressure signal distributions in the symmetry plane.

Schematics of the nozzle geometry with showing the geometrical modifications compared to the previous geometry by dashed lines.	A space-time diagram of the deck wall pressure signal in the symmetry plane
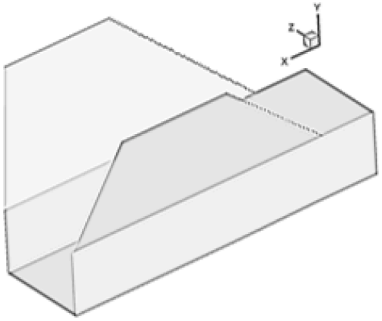 Baseline model, $f_0 = 64$ 5Hz	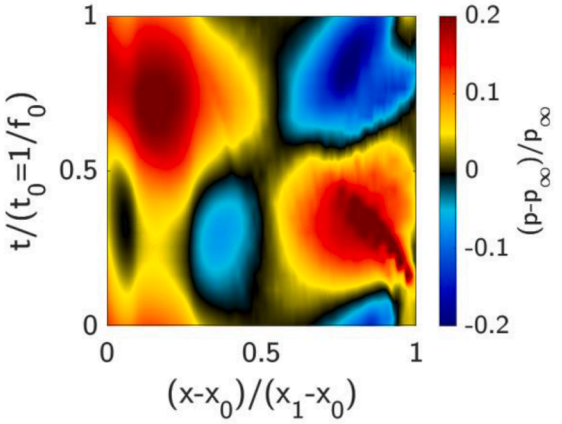
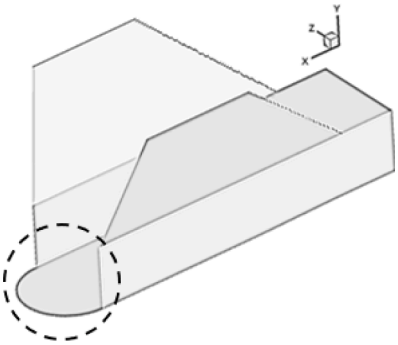 Modification A, $f_0 = 645$ Hz	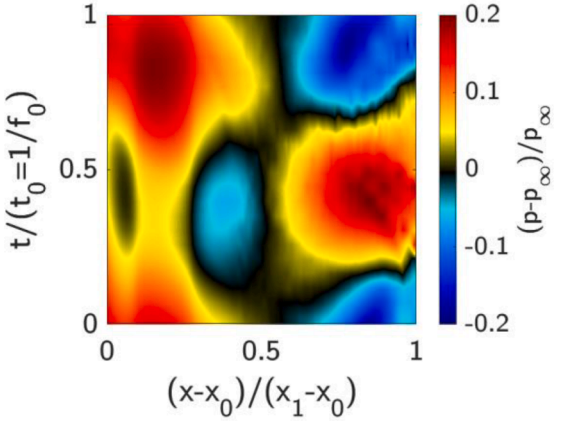
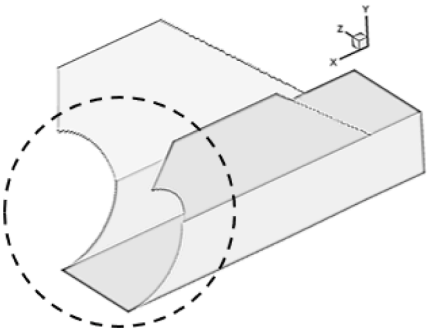 Modification B, $f_0 = 780$ Hz	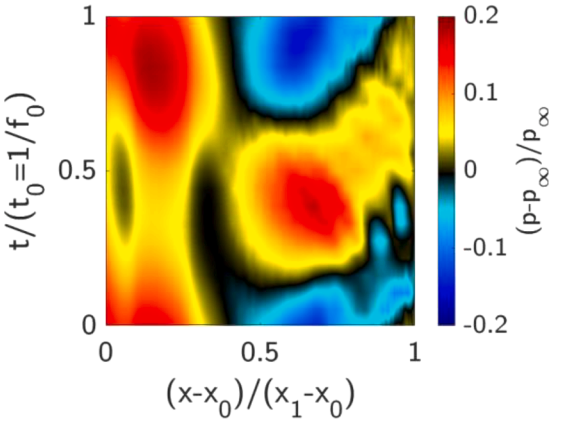

(continued on next page)

(*continued*)

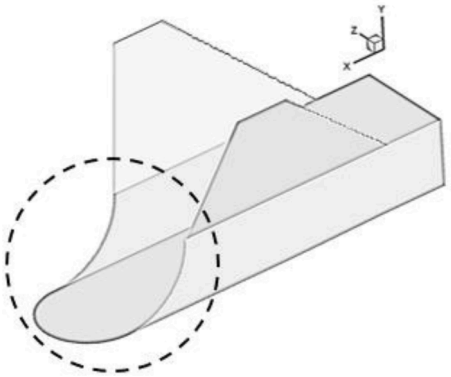

Modification C, $f_0 = 790$ Hz

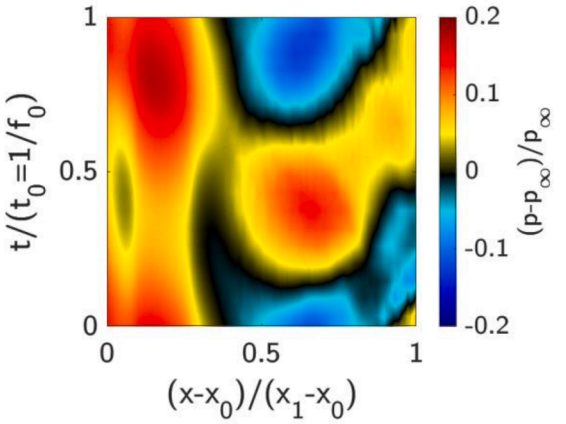

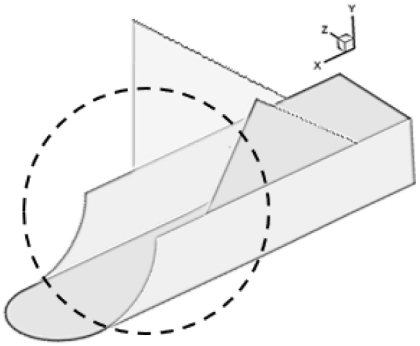

Modification D, $f_0 = 815$ Hz

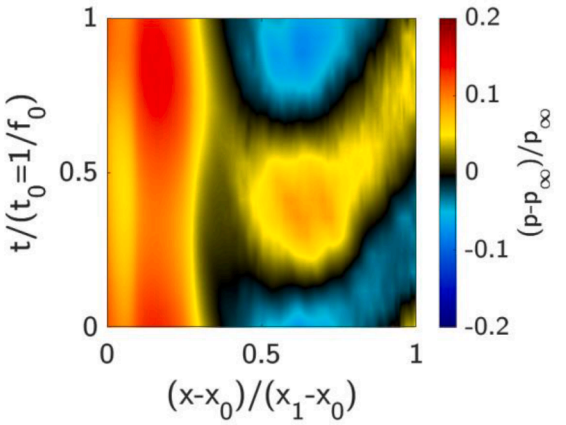

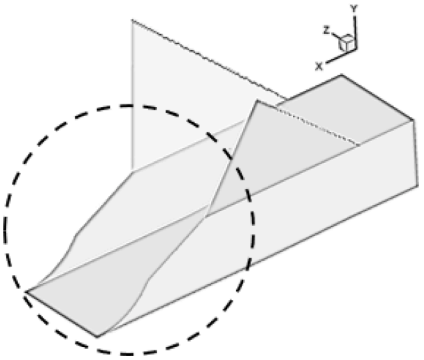

Modification E, no tone, $f_0 = 815$ Hz

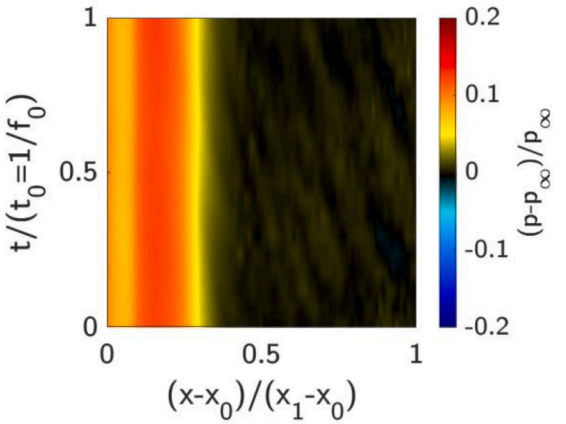

(*continued on next page*)

(*continued*)

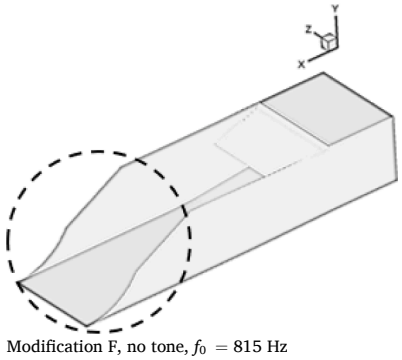

Modification F, no tone, f_0 = 815 Hz

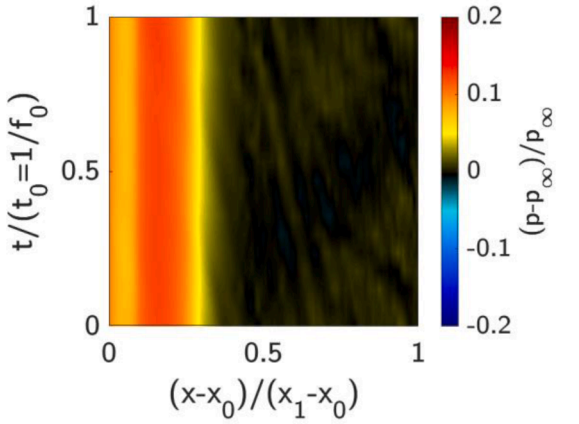

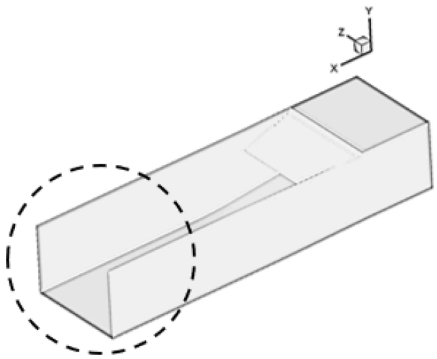

Modification G, f_0 = 815 Hz

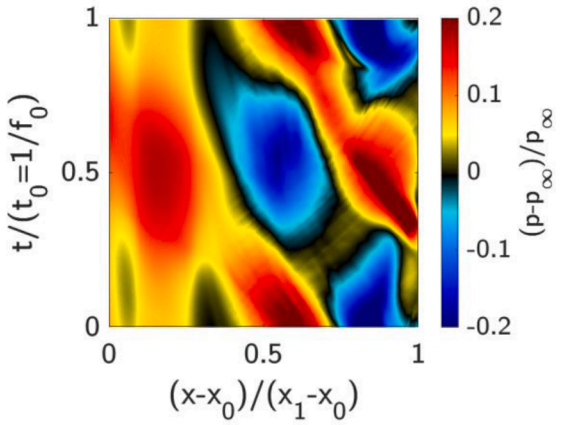

4.2. *Acoustic modelling of the installed rectangular jet for nozzle configuration with no tone and further insights*

It can be noticed that for the optimized tone-less configuration of the installed rectangular nozzle, the flow solution looks qualitatively like an isolated jet (Fig. 19b). Therefore, it can be expected that in this case the effect of the jet installation is relatively small, thereby making the installed rectangular jet acoustically similar to an isolated round jet. To quantify this, the zonal LES solution of configuration F has been combined with the FW – H method for far-field noise predictions as outlined in the previous sections. In addition to positive polar angles of the CIAM acoustic rig, which correspond to the reflected side of the installed jet ('down') (Fig. 2), noise prediction results for negative polar angles corresponding to the shielded side ('up') were also included for comparison.

Fig. 20a shows the predicted OASPL and noise spectra from the zonal LES-FW-H method with the CIAM noise measurements of the reference isolated round nozzle. Experimental data for the baseline installed square jet for the down observer angles are included for comparison. It can be noted that the predicted noise levels of the installed rectangular nozzle of configuration F are different for the reflected and the shielded side of the nozzle: the noise levels on the shielded side are 2–3 dB lower. Due to the tone elimination, the installed jet of configuration F is 5–10 dB quieter in comparison with the baseline case. At the same time, noise levels of the installed jet for the shielded microphone locations are very similar (within 1 dB) to the reference isolated round CIAM jet, which confirms the acoustic similarity of the two jet cases in this case.

Fig. 20b compares the 1/3 octave spectrum measured for the original installed rectangular jet and the isolated round jet as well as the noise spectrum computed for the optimized tone-less configuration from the LES solution. The noise spectrum was computed for a typical downstream observer angle, where a prominent main tone occurred in the original noise spectra dataset at St $\sim$ 0.2 (Fig. 15b).

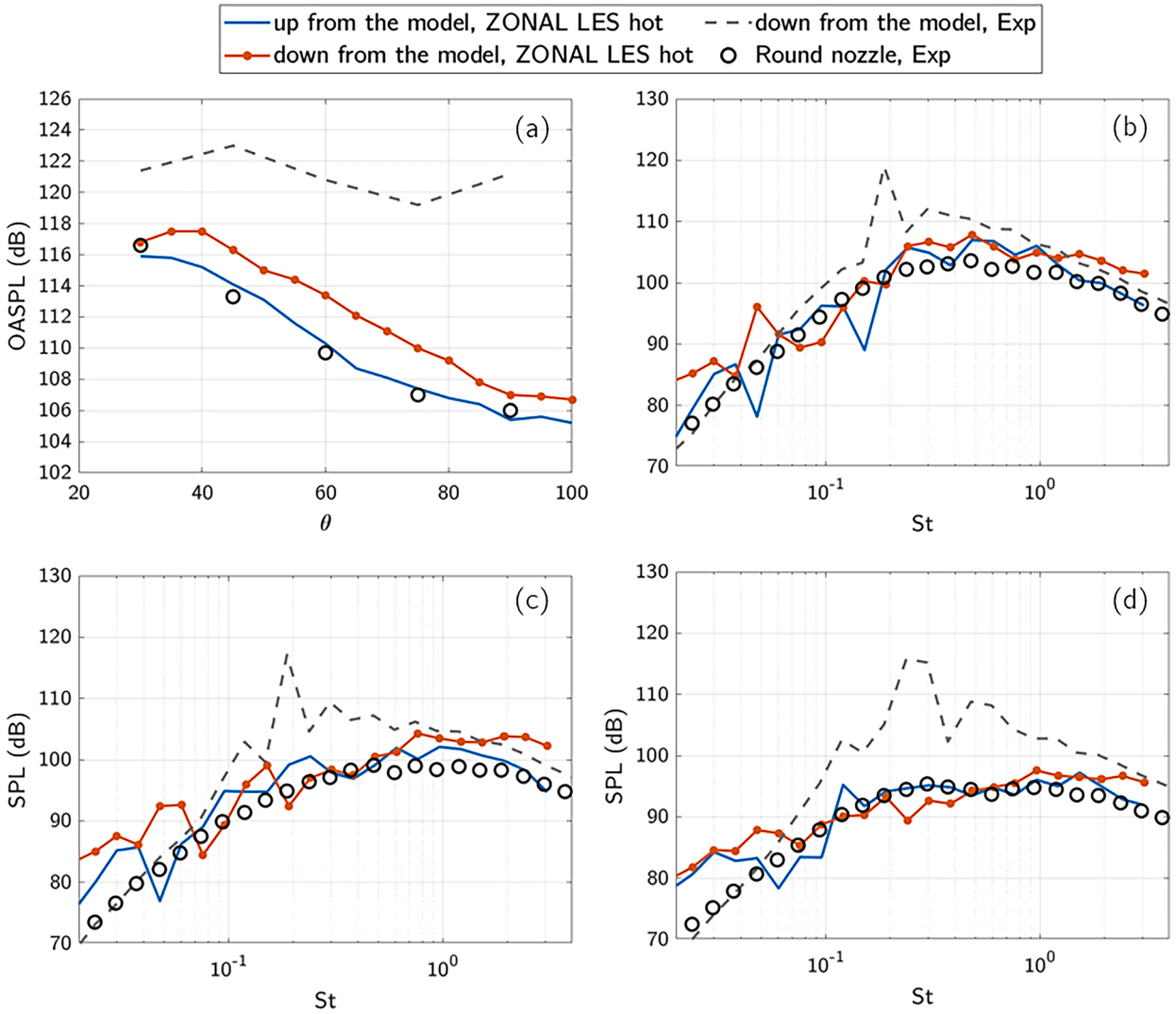

Fig. 20. Comparison of noise predictions of the zonal LES-FW-H model for the optimized installed rectangular jet (configuration F) with the CIAM measurements for the baseline installed rectangular jet and the reference isolated round jet: (a) OASPL and (b) 1/3 octave noise spectra for observer angle 45°. 'Up' and 'down' correspond to the shielded and the reflected side of the optimized installed jet, respectively.

It can be seen that the noise spectra of the optimized configuration corresponding to the reflected and the shielded side of the nozzle are completely free from the tone, in accordance with the previous analyses.

To further understand the differences between the noise generated on the reflected and the shielded side of the considered installed jet configuration, additional calculations using the conditional analysis have been performed to visualize the correlated pressure structures in the corresponding top and bottom jet shear layers of the rectangular jet (Appendix). Correlations with the control signal points located both on the reflected and the shielded sides of the jet have been considered. For the bottom shear layer downstream of the deck trailing edge, the correlated pressure waves are amplified for noise propagation corresponding to the shielded side of the jet. At the same time, for the top shear layer, which forms downstream of the upper nozzle lip and propagates through the jet embodiment geometry, the amplified pressure structures are located on the reflected part of the jet. This suggests that the difference between the optimized installed rectangular jet and the reference isolated jet is associated with the effective noise sources in the top shear layer of the installed jet on the reflected side, whilst the bottom shear layer associated with the shielded side is acoustically similar to an isolated jet.

5. Conclusions

A series of Zonal LES have been performed for the installed rectangular jet nozzle and flow conditions of the CIAM experiment using a high-resolution numerical scheme based on the fourth-order spatial flux reconstruction and the third-order integration in time. The LES and Unsteady RANS (URANS) regions are coupled using the Improved DDES framework, implementing the synthetic turbulence generator, as recommended in the previous literature.

For verification of the zonal LES approach, two zonal LES setups have been compared. In the first setup, the entire semi-closed jet flow above the deck has been modelled with URANS, which leads to significant savings of computational resources in comparison with pure LES methods. In the second setup, the development of the jet flow starting approximately one effective diameter downstream of the upper nozzle lip is modelled with pure LES, leading to an enhanced resolution of the jet flow solution at an increased computing cost. While the second approach is necessary for eddy-resolving simulations of the developing jet flow, the first approach has been found sufficient for reproducing the essential dynamics of flow resonance as confirmed by the Fourier and POD analyses.

Having established that the zonal LES model resolution is sufficient to investigate pertinent dynamics of the installed rectangular jet flow, several additional calculations are performed to analyse the nature of the resonance in the considered jet flow. In particular, it is shown that jet heating moves the tone in the jet pressure fluctuations to a higher frequency compared to the unheated jet. The increase of the tone frequency in the heated jet does not scale with the Helmholtz number, thereby suggesting the importance of acoustic-flow interaction effects.

For validation of the numerical model against the CIAM acoustic measurements, the zonal LES solution has been coupled with the Ffowcs Williams and Hawkings method implemented in the frequency domain. Because of the relatively short LES signal, first several tones were separated from the original signal. The remaining part of the signal was treated as broadband, hence, to reduce statistical noise for this signal, a multi-window Fourier transform based on the Welch averaging was applied.

Before proceeding with the acoustic solution validation, uncertainty of the CIAM noise measurements due to reflections in the non-anechoic CIAM facility has been quantified by comparing the noise spectra measurements of an isolated round jet in the same facility with the reference jet noise data from NASA. Having taken this uncertainty and the scatter of the CIAM data in comparison with the mean trendline into account, it is shown that the broadband noise component of the zonal LES-FW-H solution is broadly within the experimental error bar of the CIAM noise measurements for all angles and frequencies up to around $St \sim 2$. Furthermore, it is shown that the dominant tone of the acoustic spectra for 45° and 60° observer angles has been accurately predicted in comparison with the experiment too. For the other two angles, 30° and 90°, larger discrepancies for the predicted main tone with the experiment have been observed, which can be partly explained by a larger experimental uncertainty at low frequencies for these two polar angles as well as the insufficient LES grid resolution potentially. Far-field noise predictions of the sixth multiple of the main tone, which correspond to $St \sim 1$ are also more-or-less well captured in the calculation in comparison with the CIAM experiment apart from results for the 60° observer angle. In the latter case, the increased scatter of the experimental dataset at $St \sim 1$ is suggested as a possible reason for the bigger discrepancy between the zonal LES predictions and the CIAM measurements.

Despite the discrepancies and uncertainties mentioned, the overall agreement between the current zonal LES-FW-H solution the experiment is found encouraging, considering complexity of the installed jet flow and the modest size of the LES grid (60 million cells) compared to the current Wall Modelled LES model standards and the lack of jet LES solutions for such complex installed jet configurations in the literature.

To further analyse the pressure propagation effects in the installed rectangular jet, the zonal LES solution has been examined using spectral and conditional averaging methods. By reconstructing a numerical dispersion analysis for waves propagating in the streamwise direction between the deck trailing edge and an upstream point, two branches of the acoustic waves are obtained, which

correspond to the upstream and downstream propagation directions. It is shown that the phase speed of the upstream propagating waves tends to decay at high frequencies, while the downstream wavs are always cut-on, in consistence with upstream propagation of oblique acoustic wave in duct flows. By computing the characteristic phase speeds, the stream-wise distance between the upstream and downstream reflection points of the resonance loop is found to be significantly smaller than the length of the deck between the upstream nozzle lip and the deck trailing edge, which suggests the effect of complex oblique wave reflections in this installed jet flow.

Results of the conditional analyses based on correlations with the linear hydrodynamic field have further shown the loci of $\pm 180^{o}$ phase changes of the pressure waves inside the jet, which are interpreted as acoustic reflection points. Several of such reflections are identified in the vicinity of the bottom wall and just upstream of the deck trailing edge, thereby explaining the small values of the stream-wise distance between the upstream and downstream reflection points in the jet obtained earlier from the dispersion analysis of stream-wise pressure wave propagation. In addition to the reflection points, two saddle points were also identified, which can be related to isolated vortices downstream of the side wall edges, radiating pressure waves coherently with the dominant tone. The side wall edges were also found to correspond to wave reflection points of rapid phase changes at high frequency.

Using the acquired insights into the importance of the side wall geometry for the acoustic-flow interaction, seven modifications of the baseline installed rectangular nozzle have been implemented using the zonal LES setup 2, which resolves most part of the jet. The modified configurations have been systematically considered to separately analyse one candidate feature for closing the acoustic-flow resonance loop at a time. The first two configurations have shown that including chevron-like lobes and serrations on the trailing edges of either the deck or the side walls do not appreciably affect the resonance. Neither do the modified installed nozzle configurations, which are based on removing the top sharp edges of the triangular wall elements. At the same time, removing the sharp corners downstream of the side walls has turned out to be the correct solution for breaking the resonance cycle. This confirms that the pointed wall edges, which were identified by the conditional analysis as reflection points as well as the trigger points for the saddle source regions associated with the vorticity shedding, are most crucial for the acoustic-flow resonance cycle in the considered installed rectangular jet flow case. By the eliminating these corner points, the tone was completely eliminated, and the installed rectangular jet became very similar to an isolated jet flow. To quantify this similarity, the far-field noise levels of the optimised tone-less modification of the original installed square jet are computed in the OASPL norm as well as the 1/3 Octave Band spectra. These noise solutions are compared with the reference CIAM noise measurements of the isolated round jet and those of the baseline installed rectangular jet. The comparison shows that removing the tone makes the installed rectangular jets significantly quieter in comparison with the baseline configuration. Furthermore, noise levels on the shielded side of the tone-less installed jet are very close (within 1 dB in terms of OASPL) to the reference isolated round jet dataset. The reflected side shows some 2–3 dB amplification in comparison with shielded side. This amplification can be associated with the jet installation noise sources in the shear layer on the reflected side of the jet, as confirmed by results of the conditional analyses.

CRediT authorship contribution statement

V.A. Shorstov: Writing – original draft, Validation, Software, Investigation, Data curation, Conceptualization. **S.A. Karabasov:** Writing – review & editing, Writing – original draft, Methodology, Investigation, Formal analysis, Conceptualization. **V.E. Makarov:** Supervision, Resources, Project administration, Methodology, Investigation, Data curation. **A.K. Mironov:** Methodology, Investigation, Data curation. **V. Gryazev:** Writing – review & editing, Writing – original draft, Visualization, Formal analysis, Data curation.

Declaration of competing interest

The authors declare that they have no known competing financial interests or personal relationships that could have appeared to influence the work reported in this paper.

Acknowledgements

The study performed as part of the program for the creation and development of a World-Class Scientific Center “The Supersonic” (Sverkhzvuk) for 2020–2025 with support from the Ministry of Science and Higher Education of Russia (Grant agreement of May 17, 2022 No 075–15–2022–1023). The work of S.Karabasov and V.Gryazev also was supported by the European Union’s H2020 program under the DJINN (Decrease Jet INstallation Noise) project, Grant Agreement No 861438.

Appendix: visualisation of noise sources in a toneless installed rectangular jet

Fig. A1 shows the pressure levels computed in the symmetry plane of the installed rectangular jet configuration F after conditional averaging (see Section 4). Results for four frequency bands are shown for control point locations above and below the jet.

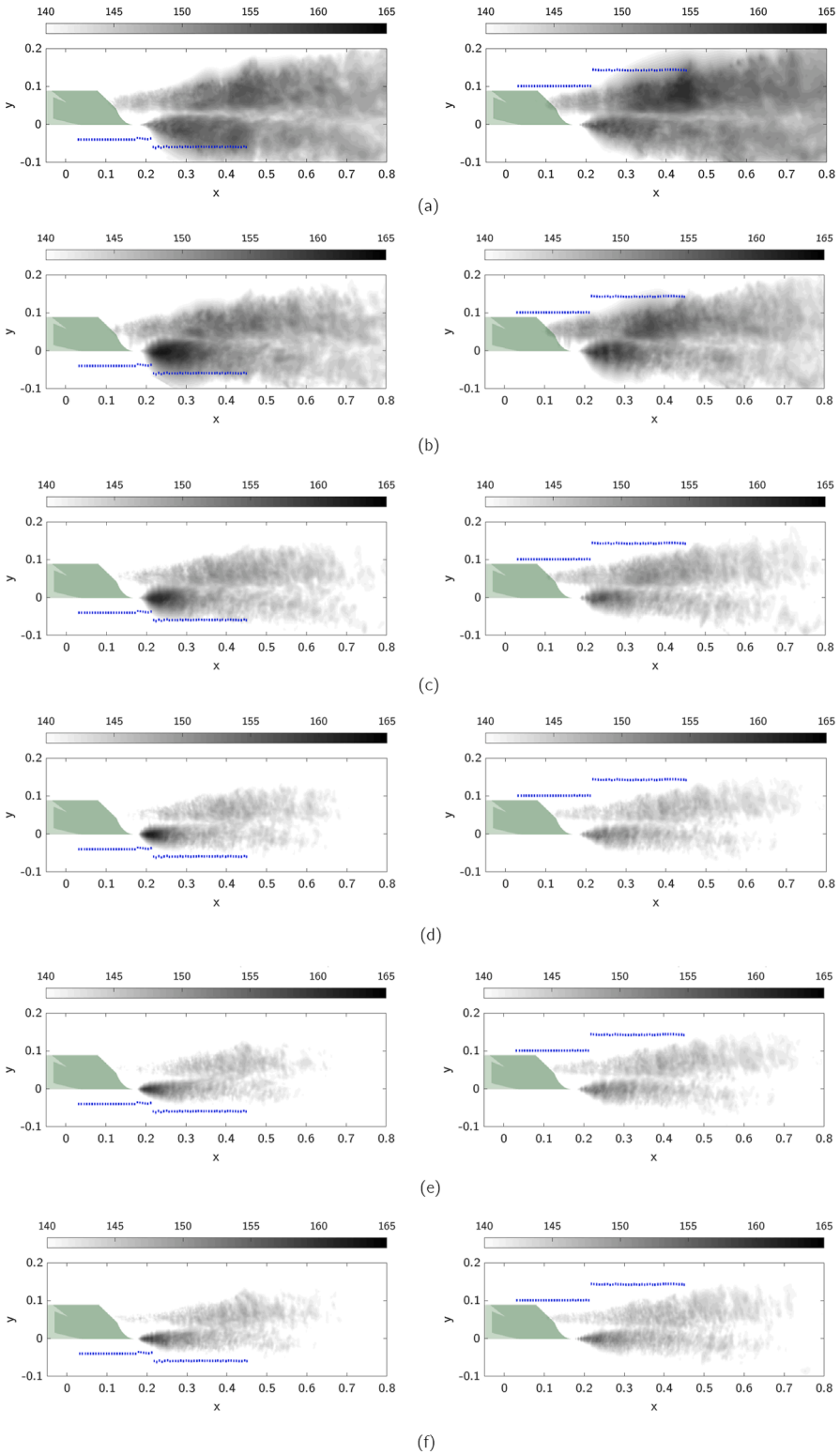

Fig. A1. Band-limited sound pressure levels in the symmetry plane of the installed rectangular jet configuration F, after conditional averaging of the pressure fluctuations. Locations of control points for conditional analysis are shown by blue symbols. Each subfigure corresponds to a different frequency band: (a) 0 - 1047 Hz, (b) 1047 Hz - 2149 Hz, (c) 2149 Hz −3225 Hz, (d) 3225 Hz - 4300 Hz,(e) 4300 Hz - 5375 Hz, (f) 5375 Hz - 6449Hz.

Data availability

Data will be made available on request.

References

[1] J.E. Bridges, C.A. Brown, R. Bozak, Experiments on exhaust noise of tightly integrated propulsion systems, in: Proc. 20th AIAA/CEAS Aeroacoustics Conference, Atlanta, GA, USA, 2014, https://doi.org/10.2514/6.2014-2904.
[2] V. Mengle, The effect of nozzle-to-wing gulley height on jet flow attachment to the wing and jet-flap interaction noise, in: Proc. 17th AIAA/CEAS Aeroacoustics Conference (32nd AIAA Aeroacoustics Conference), Portland, OR, USA, 2011, https://doi.org/10.2514/6.2011-2705.
[3] K.B.M.Q. Zaman, A.F. Fagan, J.E. Bridges, C.A. Brown, An experimental investigation of resonant interaction of a rectangular jet with a flat plate, J. Fluid Mech. 779 (2015) 751–775, https://doi.org/10.1017/jfm.2015.453.
[4] K. Bushell, Measurement and prediction of jet noise in flight, in: Proc. 2nd Aeroacoustics Conference, Palo Alto, CA, USA, 1975, https://doi.org/10.2514/6.1975-461.
[5] R. Head, M. Fisher, Jet/surface interaction noise - Analysis of farfield low frequency augmentations of jet noise due to the presence of a solid shield, in: Proc. 3rd Aeroacoustics Conference, Pasadena, CA, USA, 1976, https://doi.org/10.2514/6.1976-502.
[6] A.T. Jones, Edge tones, J. Acoust. Soc. Am. 14 (1942) 131–139, https://doi.org/10.1121/1.1916208.
[7] N. Curle, The mechanics of edge-tones, in: 216, 1953, pp. 412–424, https://doi.org/10.1098/rspa.1953.0030.
[8] A. Powell, On the edgetone, J. Acoust. Soc. Am. 33 (1961) 395–409, https://doi.org/10.1121/1.1908677.
[9] P. Jordan, V. Jaunet, A. Towne, A.V.G. Cavalieri, T. Colonius, O. Schmidt, A. Agarwal, Jet–flap interaction tones, J. Fluid Mech. 853 (2018) 333–358, https://doi.org/10.1017/jfm.2018.566.
[10] C.K.W. Tam, S. Chandramouli, Jet-plate interaction tones relevant to over-the-wing engine mount concept, J. Sound Vib. 486 (2020) 115378, https://doi.org/10.1016/j.jsv.2020.115378.
[11] A. Towne, A.V.G. Cavalieri, P. Jordan, T. Colonius, O. Schmidt, V. Jaunet, G.A. Brès, Acoustic resonance in the potential core of subsonic jets, J. Fluid Mech. 825 (2017) 1113–1152, https://doi.org/10.1017/jfm.2017.346.
[12] K.B.M.Q. Zaman, A. Fagan, M. Clem, C.A. Brown, Resonant interaction of a rectangular jet with a flat-plate, in: Proc. 52nd Aerospace Sciences Meeting, National Harbor, MD, USA, 2014, https://doi.org/10.2514/6.2014-0877.
[13] H. Kamliya Jawahar, S.A. Karabasov, M. Azarpeyvand, Jet installation noise reduction using porous treatments, J. Sound Vib. 545 (2023) 117406, https://doi.org/10.1016/j.jsv.2022.117406.
[14] J.E. Bridges, Noise from aft deck exhaust nozzles—Differences in experimental embodiments, in: Proc. 52nd Aerospace Sciences Meeting, National Harbor, MD, USA, 2014, https://doi.org/10.2514/6.2014-0876.
[15] J.E. Bridges, M.P. Wernet, Noise measurements of high aspect ratio distributed exhaust systems, in: Proc. 21st AIAA/CEAS Aeroacoustics Conference, Dallas, TX, USA, 2015, https://doi.org/10.2514/6.2015-3119.
[16] L. Rego, F. Avallone, D. Ragni, D. Casalino, Jet-installation noise and near-field characteristics of jet-surface interaction, J. Fluid Mech. 895 (2020), https://doi.org/10.1017/jfm.2020.294.
[17] S.A. Karabasov, V.M. Goloviznin, Compact accurately boundary-adjusting high-resolution technique for fluid dynamics, J. Comput. Phys. 228 (2009) 7426–7451, https://doi.org/10.1016/j.jcp.2009.06.037.
[18] A.P. Markesteijn, S.A. Karabasov, Simulations of co-axial jet flows on graphics processing units: the flow and noise analysis, Phil. Trans. R. Soc. A 377 (2019) 20190083, https://doi.org/10.1098/rsta.2019.0083.
[19] A.P. Markesteijn, S.A. Karabasov, Large eddy simulation and acoustic modelling of an installed jet configuration of industrial complexity on graphics processing units, Appl. Acoust. 224 (2024) 110159, https://doi.org/10.1016/j.apacoust.2024.110159.
[20] G.A. Brès, S.K. Lele, Modelling of jet noise: a perspective from large-eddy simulations, Phil. Trans. R. Soc. A 377 (2019) 20190081, https://doi.org/10.1098/rsta.2019.0081.
[21] V. Gryazev, A.P. Markesteijn, S.A. Karabasov, J.L.T. Lawrence, A.R. Proença, Jet flow and noise predictions for the Doak Laboratory Experiment, AIAA J. 61 (2023) 3078–3090, https://doi.org/10.2514/1.J062365.
[22] C. Horner, A. Sescu, M. Afsar, E. Collins, Numerical investigation of a rectangular jet exhausting over a flat plate with periodic surface deformations at the trailing edge, ArXiv. (2021), https://doi.org/10.48550/arXiv.2111.03478.
[23] M.L. Shur, P.R. Spalart, M.Kh. Strelets, A.K. Travin, A hybrid RANS-LES approach with delayed-DES and wall-modelled LES capabilities, Int. J. Heat Fluid Flow. 29 (2008) 1638–1649, https://doi.org/10.1016/j.ijheatfluidflow.2008.07.001.
[24] V.A. Shorstov, V.E. Makarov, Computation of aerodynamic and acoustic characteristics of NACA0012 airfoil using the zonal RANS–IDDES approach, Math. Models Comput. Simul. 11 (2019) 9–21, https://doi.org/10.1134/S2070048219010150.
[25] C. Mockett, M. Fuchs, T. Knacke, F. Kramer, Industrial prediction of jet-flap interaction noise with advanced hybrid RANS-LES methods, in: Y. Hoarau, S. Peng, D. Schwamborn, A. Revell (Eds.), Progress in Hybrid RANS-LES Modelling, Papers Contributed to the 6th Symposium on Hybrid RANS-LES Methods, 26-28 September 2016, Springer, Strasbourg, France, 2018, pp. 297–308.
[26] V.A. Shorstov, V.E. Makarov, The development of the zonal RANS-IDDES approach to simulation of flow around bodies to relax the computational requirements in computational aeroacoustics, TSAGI Sci. J. 50 (2019) 621–633.
[27] V.A. Shorstov, Development of a Numerical Method For Aircraft Powerplant's Elements Noise Prediction Based On RANS-IDDES Zone Approach (in Russian). PhD Dissertation, 2021.
[28] M.L. Shur, M.Kh. Strelets, A. Travin, A. Probst, S. Probst, D. Schwamborn, S. Deck, A. Skillen, J. Holgate, A. Revell, Improved embedded approaches, in: Go4Hybrid: Grey Area Mitigation for Hybrid RANS-LES Methods, Notes Numer. Fluid Mech. Multidiscip. Des., 134, Springer Int., Switzerland, 2018, https://doi.org/10.1007/978-3-319-52995-0_3.
[29] S.Ju. Krasheninnikov, A.K. Mironov, E.V. Pavlyukov, A.V. Shenkin, V.K. Zhitenev, Mixer-ejector nozzles: acoustic and thrust characteristics, Int. J. Aeroacoust. 4 (2005) 267–288, https://doi.org/10.1260/1475472054771448.
[30] J. Bridges, M.P. Wernet, The NASA Subsonic Jet Particle Image Velocimetry (PIV) Dataset, NASA TM-2011-216807, 2011.
[31] A. Khavaran, J. Bridges, Development of jet noise power spectral laws using SHJAR data, in: Proc. 15th AIAA/CEAS Aeroacoustics Conference (30th AIAA Aeroacoustics Conference), Miami, FL, USA, 2009, https://doi.org/10.2514/6.2009-3378.
[32] A.K. Travin, M.L. Shur, P.R. Spalart, M.Kh. Strelets, Improvement of delayed detached-eddy simulation for LES with wall modelling, in: Proc. European Conference on Computational Fluid Dynamics ECCOMAS CFD, Delft, Netherlands, 2006.
[33] P.R. Spalart, S. Deck, M.L. Shur, K.D. Squires, M.Kh. Strelets, A. Travin, A new version of detached-eddy simulation, resistant to ambiguous grid densities, Theor. Comput. Fluid Dyn. 20 (2006) 181–195, https://doi.org/10.1007/s00162-006-0015-0.
[34] P.R. Spalart, S.R. Allmaras, A one-equation turbulence model for aerodynamic flows, in: Proc. 30th Aerospace Sciences Meeting and Exhibit, Reno, NV, USA, 1992, https://doi.org/10.2514/6.1992-439.
[35] A. Suresh, H.T. Huynh, Accurate monotonicity-preserving schemes with Runge-Kutta time stepping, J. Comput. Phys. 136 (1997) 83–99, https://doi.org/10.1006/jcph.1997.5745.
[36] A. Towne, O.T. Schmidt, T. Colonius, Spectral proper orthogonal decomposition and its relationship to dynamic mode decomposition and resolvent analysis, J. Fluid Mech. 847 (2018) 821–867, https://doi.org/10.1017/jfm.2018.283.
[37] J.E. Ffowcs Williams, D.L. Hawkings, Sound generation by turbulence and surfaces in arbitrary motion, Phil. Trans. R. Soc. Lond. A 264 (1969) 321–342, https://doi.org/10.1098/rsta.1969.0031.

[38] M.L. Shur, P.R. Spalart, M.Kh. Strelets, Noise prediction for increasingly complex jets. Part I: methods and tests, Int. J. Aeroacoust. 4 (2005) 213–245, https://doi.org/10.1260/1475472054771376.
[39] D. Lockard, A comparison of Ffowcs Williams-Hawkings solvers for airframe noise applications, in: Proc. 8th AIAA/CEAS Aeroacoustics Conference & Exhibit, Breckenridge, CO, USA, 2002, https://doi.org/10.2514/6.2002-2580.
[40] R.J. Adrian, Stochastic estimation of conditional structure: a review, Appl. Sci. Res. 53 (1994) 291–303, https://doi.org/10.1007/bf00849106.
[41] F. Kerhervé, P. Jordan, A.V.G. Cavalieri, J. Delville, C. Bogey, D. Juvé, Educing the source mechanism associated with downstream radiation in subsonic jets, J. Fluid Mech. 710 (2012) 606–640, https://doi.org/10.1017/jfm.2012.378.
[42] D. Nerukh, S. Karabasov, Water–peptide dynamics during conformational transitions, J. Phys. Chem. Lett. 4 (2013) 815–819, https://doi.org/10.1021/jz400051p.